frontiers | Frontiers in Earth Science

TYPE Original Research
PUBLISHED 21 November 2023
DOI 10.3389/feart.2023.1250702

OPEN ACCESS

EDITED BY
Guillermo Booth-Rea,
University of Granada, Spain

REVIEWED BY
Karoly Nemeth,
Institute of Earth Physics and Space Science (EPSS), Hungary
Luis E. Lara,
Austral University of Chile, Chile

*CORRESPONDENCE
Daniel Mège,
dmege@cbk.waw.pl

RECEIVED 30 June 2023
ACCEPTED 02 November 2023
PUBLISHED 21 November 2023

CITATION
Mège D, Hauber E, Dyment J, Allemand P, Moors H, De Craen M and Choe H (2023), Tectonic and hydrothermal activity at the Yellow Lake fissure in response to the 2004 Dallol dyke intrusion event in Afar. *Front. Earth Sci.* 11:1250702. doi: 10.3389/feart.2023.1250702

Tectonic and hydrothermal activity at the Yellow Lake fissure in response to the 2004 Dallol dyke intrusion event in Afar

Daniel Mège[1]*, Ernst Hauber[2], Jérôme Dyment[3], Pascal Allemand[4], Hugo Moors[5], Mieke De Craen[5] and Hanjin Choe[6]

[1]Centrum Badań Kosmicznych Polskiej Akademii Nauk (CBK PAN), Warszawa, Poland, [2]Institute of Planetary Research, German Aerospace Centre (DLR), Berlin, Germany, [3]Université Paris Cité, Institut de physique du globe de Paris, CNRS, Paris, France, [4]Université Claude Bernard Lyon 1, ENS Lyon, Université Jean Monnet Saint-Étienne and CNRS, Laboratoire de Géologie de Lyon, Terre Planètes Environnement, Villeurbanne, France, [5]SCK CEN Belgian Nuclear Research Centre, Mol, Belgium, [6]Department of Geological Sciences, Pusan National University, Busan, Republic of Korea

The Danakil depression in Ethiopia, at the southern end of the Red Sea, has been the place of volcanic crises in 2004–10, with emplacement of at least 15 dykes. One of them, non-emergent, occurred in dry lake Asale next to Black Mountain and south of Mount Dallol during fall 2004. We report on the opening of a 4.5 km-long fissure in the ground at the same time the Black Mountain dyke was intruding the crust 2 km westward and parallel to it. The fissure, located north and south of Yellow Lake (Gaet'ale) and trending NNW-SSE, is still hydrothermally active. First, we describe the remarkable diversity of morphologic expressions of the fissure, made possible by development in an evaporite sequence. Satellite image monitoring reveals that its formation is coeval with the latest intrusion stage of the Black Mountain dyke. Hydrothermal activity in the fissure area is, however older than ~60 years. It is suggested that hydrothermal activity is primarily a side effect of the igneous processes, probably sill intrusion, that resulted in the uplift of Mount Dallol area, in a ~400 m thick, fluid-saturated evaporite pile. We suggest that, in 2004, emplacement of the Black Mountain dyke caused dilation within the evaporite pile overlying it, where extension was also facilitated by pressured pore fluids. This study documents the delicate intermingling of magmatic, tectonic, hydrothermal, and geomorphologic processes in evaporitic environments at the transition between continental rifting and oceanic spreading.

KEYWORDS

tectonics, hydrothermal activity, dry lake, evaporites, Dallol, Afar, Red Sea, ocean spreading centre

1 Introduction

The northern Danakil rift sits at the boundary between the Nubian Plate and the Danakil microplate (Figure 1), a transitional microplate between the Nubian Plate in the West and the Arabian Plate in the East (Eagles et al., 2002). It has attracted increased interest in the last few years owing to recent seismic crises and the polyextreme environment of Mount Dallol (Kotopoulou et al., 2019). The uniqueness of Mount Dallol lies in its salt volcanism, developing above, and triggered by, an underlying igneous complex (e.g., Otálora et al.,

2022). The top of the edifice lies at 80–90 m below sea level. It formed in dry lake Asale, where many other, much smaller, hydrothermal and halokinetic manifestations are observed (Figure 1B), but have only been partly studied (e.g., Vereb et al., 2020).

We report on a hydrothermal fissure, the Yellow Lake Fissure (YLF), located in lake Asale south of Dallol. The YLF has not been described so far. We document the diversity of geomorphological manifestations, a consequence of the specific evaporitic environment. We argue that, its tectonic and hydrothermal significance is major, being nearly parallel to the NNW Danakil depression trend and parallel to an inferred dyke interpreted to have propagated from Mount Dallol in 2004 (Nobile et al., 2012), located 2 km to the west. The YLF is also parallel to the Dabbahu-Manda Hararo dykes and rift segment. It is therefore one of the few indicators of the extensional processes occurring in the Danakil rift north of Erta ‘Ale and south of Dallol, where plate kinematics and the mechanisms of transition from continental rifting to ocean formation remains challenging (Augustin et al., 2021; Hurman et al., 2023).

2 Earlier works

North of Mount Dallol (Figure 1), a seismic swarm was recorded near Bada in December 2022, and interpreted as a consequence of plate spreading by pure tectonic extension (La Rosa et al., 2023). A seismic swarm had occurred at the same place in 1993 (Ogubazghi et al., 2004; La Rosa et al., 2023), and rupture propagation was found to be reminiscent of associated dike propagation (Ruch et al., 2021).

In the Mount Dallol area, the last major magmatic-tectonic event occurred in October-November 2004, when a dyke intruded the Danakil rift parallel to its axis in the Asale dry lake, just south of Mount Dallol and east of Black Mountain. Seismic data and InSAR modelling suggest that the Black Mountain dyke intruded the crust at a depth of 2–6 km, over a lateral distance of 9 km, with a maximum opening of 5 m at depth ~4 km. A Mogi source was identified at a close distance to the centre of Mount Dallol, at depth 1.5–3.3 km (Nobile et al., 2012).

Several months earlier, a dyke had intruded the Erta ‘Ale volcano 75 km south of the Black Mountain dyke (Barnie et al., 2016a), but its small size, extent, and shallowness make it difficult to connect to the crustal dilation materialised by the Black Mountain dyke. A year later and 175 km to the South, in September 2005, a dyke intruded south of the Dabbahu volcano, at the northern end of the Manda Hararo rift, and gave birth to a spectacular elongated vent (Wright et al., 2006). It was followed by 13 other dyke intrusions, including three eruptive, along the Manda Hararo rift (Belachew et al., 2014), the last intrusion occurring in May 2010 (Barnie et al., 2016b). Based

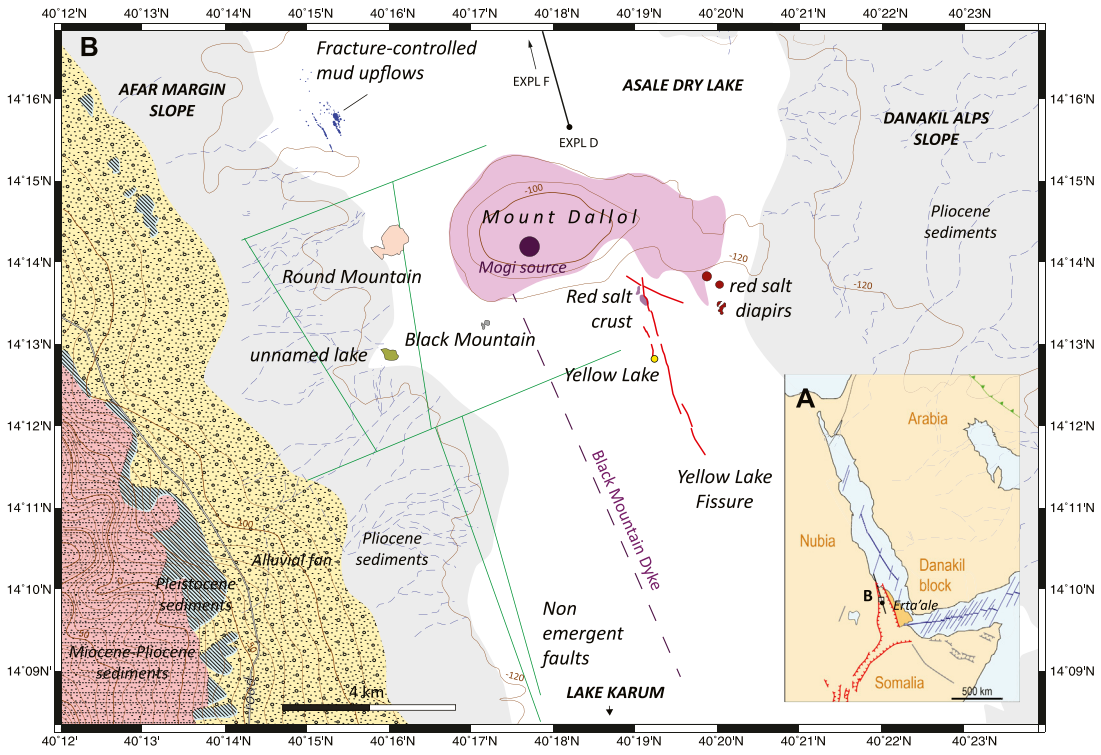

FIGURE 1
Tectonic context of the Yellow Lake Fissure (YLF) area. **(A)** Regional setting (data compiled from Bosworth et al., 2005; Hagos et al., 2016; Leroy et al., 2012; Mège et al., 2015; Wolfenden et al., 2004). The main tectonic features are located, including the northern Afar rift (black lines), spreading ridges (blue), the East African Rift (red), the main Cenozoic sedimentary basins and major dyke swarms (grey), and the Zagros frontal thrust (green). **(B)** Map of the study area, including the main tectonic and hydrologic features. Blue dashed lines are ephemeral streams. Faults are provided as interpreted from seismic reflection data (Rauche and van der Klauw, 2015). The location of the dike and Mogi source are after Nobile et al. (2012). Mount Dallol (pink) may have formed in response to sill emplacement (López-García et al., 2020). Geological formations are from Hagos et al. (2016) and include (red) the Miocene-Pliocene Red Beds sandstone; (blue) Pleistocene diatomite and gypsum; (yellow) Pliocene alluvial deposits, and evaporate and fine grained sediments. Topographic contours are inferred from the SRTM V3 1-arcs resolution digital terrain model (Farr et al., 2007). “EXPL D” and the line starting from it locate the seismic profile reproduced as Supplementary Figure S8.

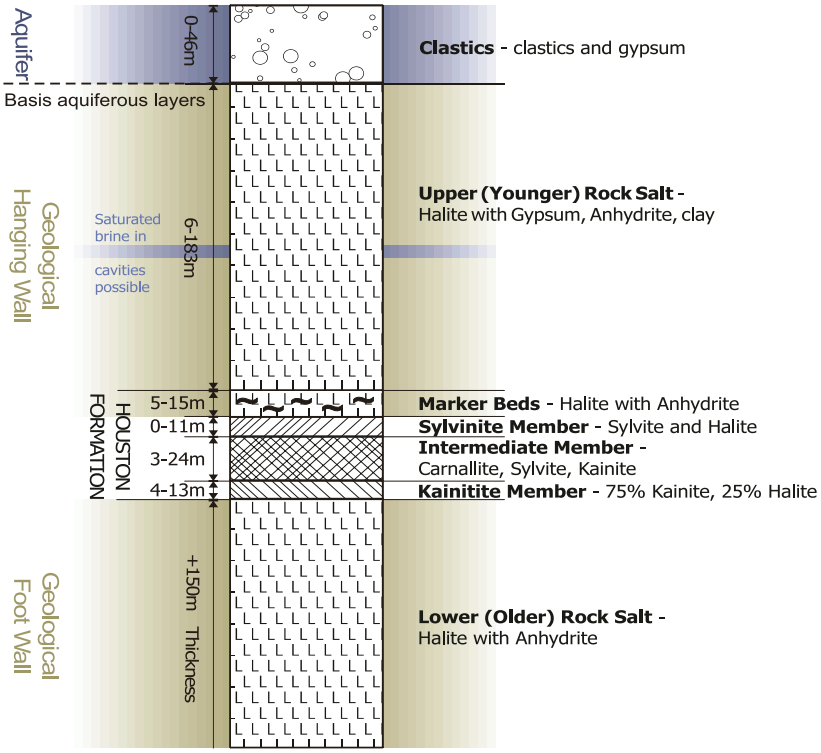

FIGURE 2
Stratigraphy of evaporite deposits in the Musley area, west of Mount Dallol. Rauche and van der Klauw (2015).

on modelling of InSAR-derived deformation and seismicity, dyke depth was from 0 km or shallow to 10 km, and length between 10 and 60 km, with a maximum opening of 0.7–3.1 m (Ebinger et al., 2010 for the 13 first intrusions; Barnie et al., 2016b for the last intrusion). Additionally, in May 2000 a deep (6–12 km), 6 km long and 1.5 m wide dyke, intruded the crust 460 km in the South, at the boundary zone between the Ethiopian Rift and Afar, in the Ayelu-Amoissa volcanic complex (Keir et al., 2011). Remote sensing analysis of the 2017–2019 Erta 'Ale volcanic crisis and InSAR inversion testifies to the continuous magmatic activity within the volcano and underneath, in the rift crust, between 2014 and 2019. This volcanic crisis included the emplacement of three well-characterised dykes along the rift during the period 2014–2017 (Moore et al., 2019).

Most of the geologic work around Mount Dallol has been conducted for potash mining. Seismic profiles were obtained and holes were drilled by the mining companies operating on Dallol and in its vicinity. Most data have been acquired on the western side of the Danakil depression, along the margin with the uplifted continental basement. South of Dallol, seismic profiles have been obtained by Allana Potash parallel and perpendicular to the Danakil depression. North of Dallol, profiles have been obtained by Circum Minerals and Yara Dallol. More than 300 holes were drilled by the Ralph M. Parsons Company in the 60s (Holwerda and Hutchinson, 1968), and were complemented by 88 holes by Allana Potash and Nova Potash. Data and analysis of many drill holes, as well as Allana seismic profiles, have also been disclosed (Rauche and van der Klauw, 2015), and combined with additional data, were used to infer geodynamic interpretations (Bastow et al., 2018). These data indicate that salts occupy the upper hundreds of meters in the rift stratigraphy at least, and probably more than 2 km locally, with increasing thickness from the western margin eastwards. The lower part of the sequence, when attained by the drill holes, includes the Lower Rock Salt, and the upper part, the Upper Rock Salt. In between, an intermediate member, the Houston Formation, includes several tens of meters of potash layers capped by the Marker Beds, a halite and anhydrite level disconformable with the Upper Rock Salt formation (Holwerda and Hutchinson, 1968; Rauche and van der Klauw, 2015). The lowermost part of the sedimentary pile, rarely attained in the drill holes, shows clays and conglomerates (Figure 2). Based on isotope ratios, the whole sequence has been ascribed a Pleistocene age (Lalou et al., 1970).

The igneous context, in particular, the depth of the intrusive source explaining the observed hydrothermal activity in Mount Dallol and surrounding areas, has been understood various ways. On the one hand, Otálora et al. (2022) suggested that Mount Dallol is a salt volcano, with mineralogical processes controlled by magmatic heat from a magma source located a couple of kilometres underneath. Because seismic profiles south of east of Dallol acquired for Allana Potash (Bastow et al., 2018) do not provide evidence for a magma body at maximum seismic profile depth, ~1.2 km, they suggest that it lies deeper, at, e.g., 2.5 km, which according to Nobile et al. (2012) is the depth of the Black Mountain dike Mogi source. On the other hand, Warren (2015) described, alternatively, how Mount Dallol may have been uplifted in response to dyke intrusion piercing the Lower Rock Salt, flattening to a sill in

the Houston Formation, at the level of the Potash Beds. This interpretation does not contradict the seismic interpretation of Bastow et al. (2018) because the seismic lines do not cross Mount Dallol itself. López-García et al. (2020) also favour the sill-intruded salt interpretation, and argue from chronostratigraphic constraints using the Afrera Formation further south in the Danakil depression as a Dallol evaporite sequence analogue that the Dallol sill must have been injected later than 6,000 years ago and is still hot.

Due to seasonal flooding by ephemeral streams eroding the neighbouring highlands on both sides of the rift (Figure 1B), and in agreement with the field observation that the water table is in general not farther than a few centimetres below the surface, Lake Asale can be considered as permanently saturated (Talbot, 2008). Groundwater circulation has been investigated by Anderson and Goode (2017), who highlighted the supply of fresh water from the neighbouring mountains in the West in the shallow subsurface, and brackish and salty waters at greater depth, which is thought to be responsible for karstification of the Upper Rock Salt. Flooding of the floor of the dry lake surface and re-evaporation generates salt redeposition in the form of a widespread thin layer of white salt crystals. Heating of the sediments by underlying magmatic activity has been suggested to generate vigorous halokinetic movements within the whole sedimentary pile (Talbot, 1978), leading to solid-state convection (Talbot, 2008; Anderson and Goode, 2017). Such patterns are yet to be reconciled with the apparently undisturbed Houston Formation sampled in the drill holes and the seismic profiles.

The resolution of the first air photograph presented in the scientific literature that shows the Dallol area (Holwerda and Hutchinson, 1968) is too coarse to identify any structure that would correspond to the YLF. One of the YLF segments, photographed in 2012, is displayed in Figure 10 in Franzson et al. (2015), who described it as a tectonic fracture. The YLF is included in the geologic map discussed by López-García et al. (2020), and the chemical and microbiological analysis of its fluids is presented in Moors et al. (2023). From satellite imagery, the thicknesses of the seasonal floods in the YLF area probably rarely exceeds 10 or 20 cm (Choe et al., in preparation). They rejuvenate the surface of the salt plates at the bottom of Lake Asale with new salt, and contaminate the fissure and hydrothermal pools with fresh surface water (Anderson and Goode, 2017).

We named the fissure after a lake located next to the central part of it, also known as Oily Lake, or improperly (according to local people) Gaet'ale. Yellow Lake is known for CO_2 release (Master, 2016) and exceptionally high dissolved salt content (Pérez and Chebude, 2017). Albino and Biggs (2021) found subtle (~1 cm) modification of the Yellow Lake topography between 2015 and 2020 in an InSAR study.

3 Data and methods

3.1 Field work

Geological data were collected in the field during a two visits to the Mount Dallol area on 21–25 January 2018, and 12–22 January 2019. They include observations of geomorphology, structural features, and evidence of hydrothermal activity, and also acquisition of magnetic data which will be presented elsewhere.

3.2 Acquisition and analysis of UAV-based topography

Topography acquired by satellite (such as from the Shuttle Radar Topography Mission and the ASTER Global Digital Elevation Map) are not adapted to the study of areas in which topographic variations are below 1 m metre. For this reason, a UAV-based survey of imagery acquisition was implemented during the 2019 campaign for stereoscopic processing. Flight altitude above ground was 100 m, images were tagged in geographic coordinates with the WGS84 datum. They were then projected to the WGS 84 / UTM zone 37N - EPSG:32637 projected coordinate system; topography was calculated and an orthorectified image generated using the MicMac[1] photogrammetric suite (Rupnik et al., 2017). The obtained pixel size is 0.5 m. Subtle vertical topographic variations < 1 m can be detected using pixel elevation averaging (such as presented here) and other statistical methods (Choe et al., in preparation).

3.3 Remote sensing data analysis

Most of the images taken by civilian and declassified satellites in the visible and near-infrared ranges until 2020 were examined for this study, as well as a subset of images obtained between 2020 and 2023. Those who were found the most useful for this study are listed in Supplementary Table S1. High-resolution images from KeyHole-4B, OrbView-3, Pleiades-1A/B, QuickBird-2, Spot-6, and WorldView-2 were used to map the details of the YLF and associated features at irregular time steps. The benefits of 10–30 m resolution data from ASTER and Landsat-7 lie in their spectral capabilities, making identification of potential surface composition variations between two consecutive passes, usually not more than 1 or 2 months. They were used to determine the succession of events at the time of YLF formation, in 2004–2005 (Supplementary Table S2).

Moreover, the thermal channels of Terra/ASTER were useful to identify possible surface temperature variations associated with the hydrothermal activity of the YLF, both diurnal, and between different orbits. Sentinel 2A/B data were also analysed, but did not yield information not already available using data from the other multispectral satellites. The YLF is nearly fully covered by four 1x1 km pixels from the Terra/MODIS Land Surface Temperature dataset. In spite of this coarse resolution, surface temperatures are measured daily, during day time and night time, making it possible to monitor whether or not development of the YLF in 2004–2005 was associated with significant thermal anomalies at surface.

Satellite images having visible and near-infrared channels were studied with conventional processing for geologic interpretations. Initial files were selected in a radiometrically corrected and projected

1 https://micmac.ensg.eu, consulted 26-08-2023

format, provided by the source image providers. Panchromatic images were enhanced through histogram stretching. Multispectral images were studied under various colour composite combinations. If the number of bands exceeds 3, various combinations were tested so as to reveal optimal rock composition contrasts. The presented image corresponds to this particular band combination, to which histogram stretching was applied in order to emphasize the contrasts. Infrared bands revealed particularly useful due to spectral variations in rock reflectance in this range, whereas visible wavelengths are devoid of major mineral absorptions. The captions indicate which bands were selected in the corresponding figure. In case both a panchromatic sensor and a multispectral sensor exist, pansharpening of the multispectral channels was done using Gram-Schmidt pansharpening (Laben and Brower, 2000; Maurer, 2013).

A composite (red-green-blue) image showing the difference between two measurement times (t_0, "before," and t_1, "after" the studied event) was generated by subtracting a given band at t_0 from the same band obtained at t_1 and attributing it to the red channel, and doing the same for two other bands and the two other channels.

Thermal information was directly retrieved from the ASTER L2 Surface Kinetic Temperature distributed by the USGS Land Processes Distributed Active Archive Center. The ASTER five thermal infrared channels were used, after atmospheric correction, to determine surface radiance. Surface radiance data were then used to generate emissivity data, from which temperature is derived.

Image processing was done using ENVI 5.5 and ENVI 5.7 (NV5 Geospatial Solutions, Inc., Broomfield, Colorado, U.S.), and the GIS part using Global Mapper 20 to 24 (Blue Marble Geographics, Hallowell, Maine, U.S.).

3.4 Water sampling and geochemical analysis

Fluids were collected at two hydrothermal pools and at Yellow Lake. The samples were collected by completely immersing autoclaved sterile glass tubes. Water temperature, pH and conductivity were measured. After sampling, the glass tubes were hermetically closed with a thick rubber sealing septum. To prevent unwanted leaking or external contamination further, the flasks were firmly sealed by forcibly crimping of an aluminium closure ring on top of the septum. After transport towards the laboratory, the samples were treated and chemically analysed as in Moors et al. (2023).

4 Results

4.1 Descriptions

4.1.1 YLF structure

The most precise structural geometry, obtained in 2005, reveals seven main segments (Figure 3). In addition, a 200 m long double segment was hydrothermally active west of the main fissure system and north of Yellow Lake. At segment 1, the YLF broadened to three parallel parts, and intersected a poorly expressed, NW-SE-trending structural trend. In the field, the YLF did not display any fresh structural features such as tension fractures or normal faults; however, its opening, with no visible vertical wall displacement, makes it a probable mode-I crack system.

4.1.2 Geomorphology

Fissure geomorphology reveals a remarkable diversity of features. Each segment has a dominant geomorphologic expression, which may vary with time (some major changes were noted between January 2018 and January 2019) but several geomorphologic types are found in most segments. They are also observed in the northern YLF area, where the N-S YLF network crosses a NW-SE fracture system, resulting in diffuse hydrothermal activity.

4.1.3 Pools

Some fissure segments are open and partly filled with hydrothermal fluids, sometimes containing ascending gas bubbles (Figure 4). These pools are usually less than 1 m long, but a few of them are a few meters long. Franzson et al. (2015) show that in 2012 water was present in at least one much longer fissure portion. A 1.50 m long rod fully penetrated the water of the largest pool found in 2018 and 2019 (Yellow Pool, Figure 3) and did not meet the bottom of the open part of the fissure. Like at Yellow Lake (e.g., Masters, 2016), dead birds are sometimes observed on the margin of the pools, interpreted as a consequence of CO_2 emissions in quantities enough to suffocate them.

4.1.4 Ridges

The surface of Lake Asale in the YLF area comprises polygonal salt plates several centimetres thick. These salt plates display various types of topographic ridges. Supplementary Figure S1 provides examples. Such patterns are also found in other places on Earth. In particular, Jackson et al. (1990) describe similar salt polygons (*namak sefid*) separated by upwelling salts in the Great Kavir, Iran. Along YLF segments, upflows bring clays to the surface at plate edges along a broken line, where they form clay ridges, termed "dry mud dykes" in Great Kavir by Jackson et al. (1990). In other areas, the salt plates are sharply broken and tilted, forming triangular-shaped, tepee-like (Talbot, 2008) fractured landforms. Clay ridges and the rotated and fractured plates are sometimes associated in a way that suggests causal relationships. Jackson et al. (1990, p. 9) mentioned the occurrence of *kaseh* in Great Kavir, which are probably similar features, forming sharp-edged salt plate pinnacles up to 1 m high, interpreted to form when radiant heat from the Sun passing through the salt is absorbed by an underlying dark salt mud, which expands thermally and oozes upward through the salt plate cracks. This mechanism probably applies here too to some extent, with a mud level observed just below the salt plates. However, the usual alignment of this morphology with the YLF suggests that here, some subsurface control is necessary to explain the observed morphology. In Lake Asale, heat of magmatic origin and mud advection might contribute to clay ridge formation and plate desiccation as well.

4.1.5 Other salt plate modifications

Other surface manifestations of hydrothermal activity occur within the salt plates or at the boundary between plates. These features are mostly north of Yellow Lake, in the area that was

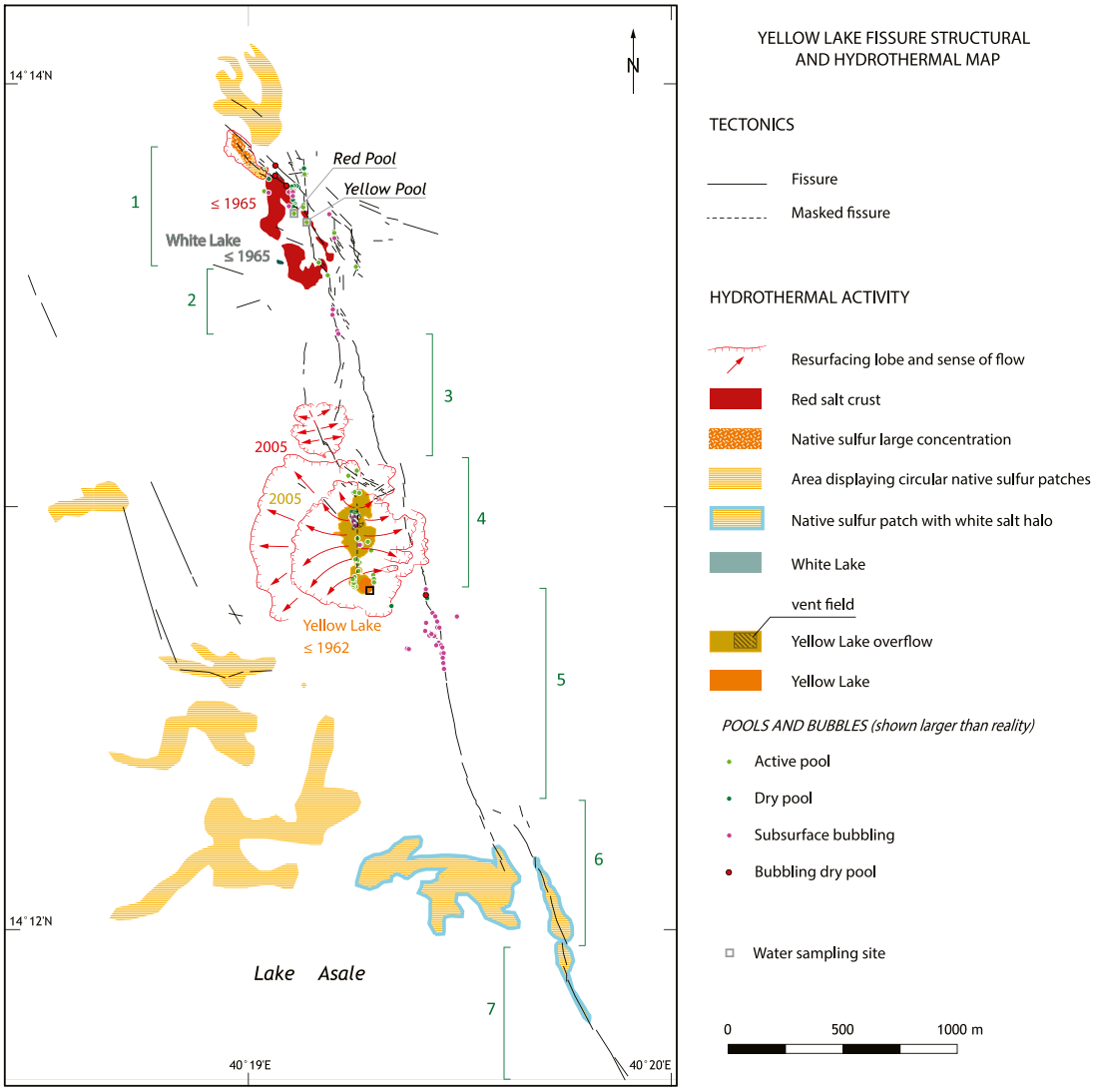

FIGURE 3
Yellow Lake Fissure structural map. The main structural segments are numbered according to the description in Section 4.1.6. Red salt outcrop boundaries were mapped after Pleiades image, 2017-10-21. Yellow Lake overflow and the extent of the resurfacing lobe in the Yellow Lake area were mapped from their original extent visible on OrbView-3 image (1 m/pixel), 2005-12-17. Fissure resurfacing in the northern area was tracked from 2005 but was mapped from Pleiades (0.5 m/pixel), 2012-11-15. The surface area of Yellow Lake was taken at its maximum extent (4,200 m^2), measured on a QuickBird image (0.33 m/pixel), 2003-06-02. Historic pool data are from the images mentioned above, plus other data from Pleiades (0.5 m/pixel) and Spot-6 (1.5 m/pixel) distributed between 2012 and 2019. Native sulphur deposition mostly occurs in circular patches, which are here usually mapped as patch fields representative of the exposures in the period 2018–2019. Chimney fields, active and dry pools, and bubbling areas refer to observations made in January 2018 and 2019. The fissures are a synthesis of observations on all the satellite images mentioned above. The masked fissure is inferred from alignment of hydrothermal features. White Lake is observed as a single body in 2003, but as two smaller lakes in the earlier high resolution imagery (1972, KeyHole-4B, 2 m/pixel, 1965, KeyHole-4A, 2.4 m/pixel).

flooded in 2005 (Figure 3). They are also observed along the YLF, although much less frequently. Supplementary Figure S2 provides examples of the common morphological features, which may combine and form complex features. Instead of forming ridges, clays expanding at the junction between three plates appear to accumulate as diapiric structures. Some plates show a circular hole surrounded by a halo of halite crystals, and sometimes small-scale radiating contractional structures. Contraction suggests that hole formation might have been accompanied by uplift, after which subsidence and hole shrinkage occurred. Holes are sometimes used as nucleation points for fractures, or as exit points of sediment accumulating around them from surge deposits. White and fragile, salt-encrusted bubbles with diameters up to a few centimetres in diameter are sometimes observed to condensate above the holes. Instead of holes, broader craters with elevated rims may form. Salt plates may be perforated by aligned holes, perhaps a preliminary to the development of new fractures that subdivide a polygonal plate to a number of smaller polygons typically bounded by a salt recrystallization margin. Resurfacing by dark clays can sometimes affect an entire polygonal plate.

In many instances, the YLF is replaced by an alignment of polygons which are broader than usual, some of them showing venting through small chimney fields. Frequently, bubbling sounds

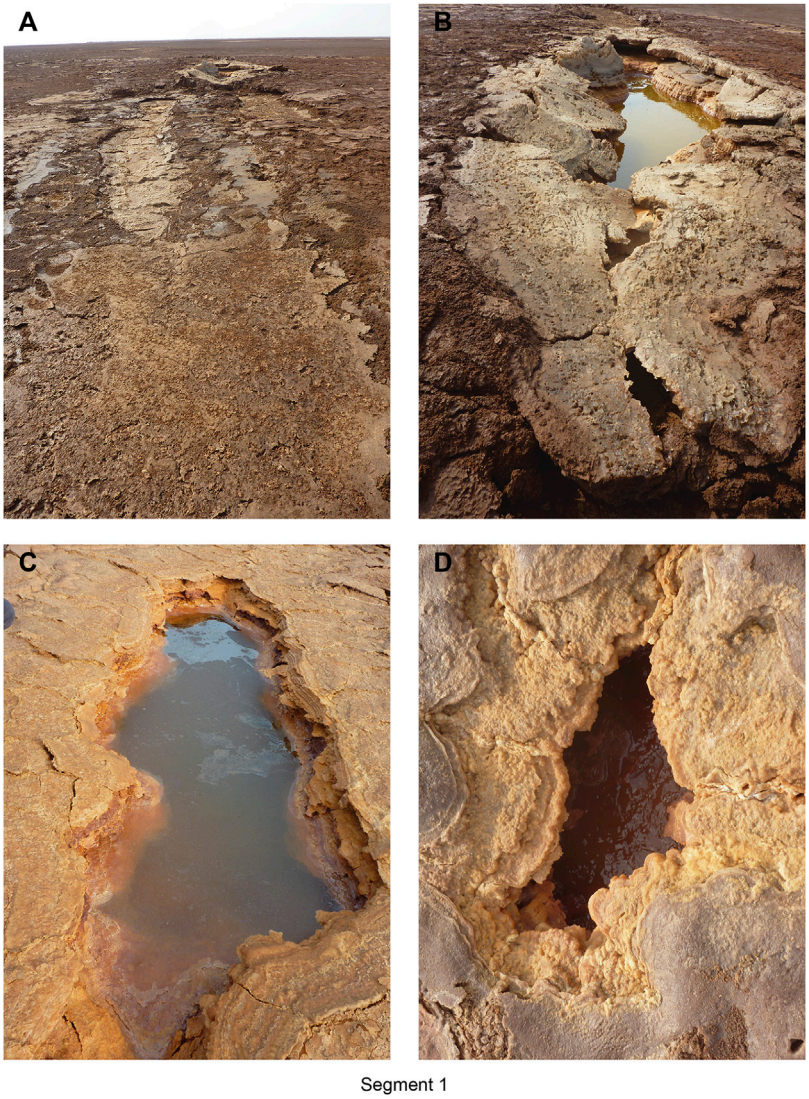

FIGURE 4
Typical morphologies of Yellow Lake Fissure along segments 1, north of Yellow Lake. Similar fissure morphology is observed along Segment 2. **(A)** Salt-covered fissure (segment 2 on Figure). The fissure locally splits into two parallel fissures, which then merge and hosts a pool in the background; **(B)** fissures in the northerly segments contain hydrothermal pools oriented along the fissure. This view shows Yellow Pool (Table 1), the largest pool identified in 2018–2019, also visible in the background in **(A)**. The hydrothermal fluids contain bubbles at the far end of the pool; **(C)** oil-film like appearance of the hydrothermal fluid in one of the pools is due to the large concentration of dissolved salts; **(D)** some pools are bubble-rich, like the Red Pool (Table 1), showed here, whereas some others, not always more distant than 10–20 m, are not bubbling at all. Photographs taken in January 2018.

can be heard from the chimneys. There are no open holes underneath in which bubbles would be seen; and the precise location of the heard bubbles remains unidentified. Venting is sometime associated with platy dark clay resurfacing. Rarely, these larger polygons are soft and sticky, and are associated with small brown mud resurfacing patches. Radial fracturing along the margins of these mud patches suggests that mud emplacement exerts some traction at the surface.

4.1.6 Segment characterisation

Supplementary Figure S3 illustrates the diversity of segment morphologies when the fissure is not visible as an open fracture at the surface.

Segments 1 and 2

Segments 1 and 2 show most of the pools observed along the fissure. The area is however structurally more complex, because it meets another, NW-SE oriented fracture zone. The surface is either composed of white salt, a red muddy, soft and sticky broad continuous salt patch, or a red salt crust (Figure 5). A vigorously bubbling salty lake collects near-surface water (Figure 5A). In its northwesterly part, approaching Mount Dallol, the red salt crust is fractured into plates the boundaries of which are filled with native sulphur deposits (Figure 5B–C). The northern part of Segment 1 is filled with white salt within the broad red muddy area. Segments 1 and 2 are the most active in the YLF hydrothermal system.

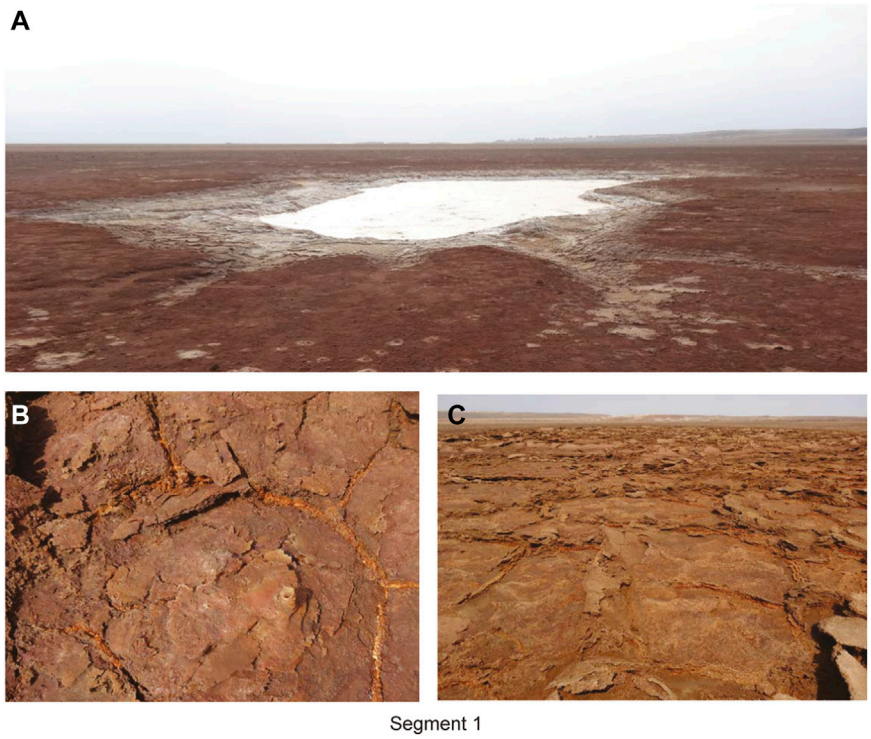

FIGURE 5
Small-scale morphology of the area of segment 1. **(A)** Vigorously bubbling lake (White Lake on Figure 2). The presence of bubbles, presumably of CO_2 composition, indicates results from degassing, whereas the many small streams converging toward the lake collects shallow surface water; **(B, C)** Native sulphur deposits along plate edges. Photographs taken in January 2019.

TABLE 1 Location of the sampling sites and properties of the sampled fluids. Yellow Pool and Red Pool are located along Segment 1 of the YLF. Conductivity and pH are measured in lab at 25°C. López-García et al. (2020) additionally identified carnallite at Yellow Lake.

	Yellow pool	Red pool	Yellow lake
Latitude	14.2279°N	14.2282°N	14.2134°N
Longitude	40.3189°E	40.3184°E	40.3214°E
T (°C)	32.0	35.1	41.2
pH	3.7	3.5	3.4
Conductivity ($mS.cm^{-1}$)	395	494	598
Minerals	Halite	Sylvite	Halite, Sylvite
	Tachyhydrite	Carnallite	Tachyhydrite
			Chloromagnesite
Dominant cations (based on mass%)	$Ca^{2+}>Na^{+}>Mg^{2+}>K^{+}$	$Ca^{2+}>Mg^{2+}> K^{+}>Na^{+}$	$Ca^{2+}>Mg^{2+}>Na^{+}>K^{+}$

Segment 3

Segment 3 is divided into a western and an eastern part. The western part is exposed as broad salt plates pierced by many small chimneys such as in Supplementary Figure S2A. The eastern part is mainly visible as linear brown clay ridges.

Segments 4 and 5

These segments are mainly marked by broad flat plates pierced by chimneys. The northern part of Segment 4, however, is observed as linear clay ridges. The transition zone between these segments is marked by broad, circular salt plates. Close to the relay zone linking the segments 4 and 5, Segment 5 displays a few small pools in which salt brines may simply show the shallow groundwater level. Such pools are restricted to this relay area between segments 4 and 5, in contrary to chimneys, which testify to active subsurface processes distributed over the whole length of these segments. Pool location in the relay zone may denote relay zone fracturing structural control; nevertheless, most pools in the YLF are not observed in relay zones,

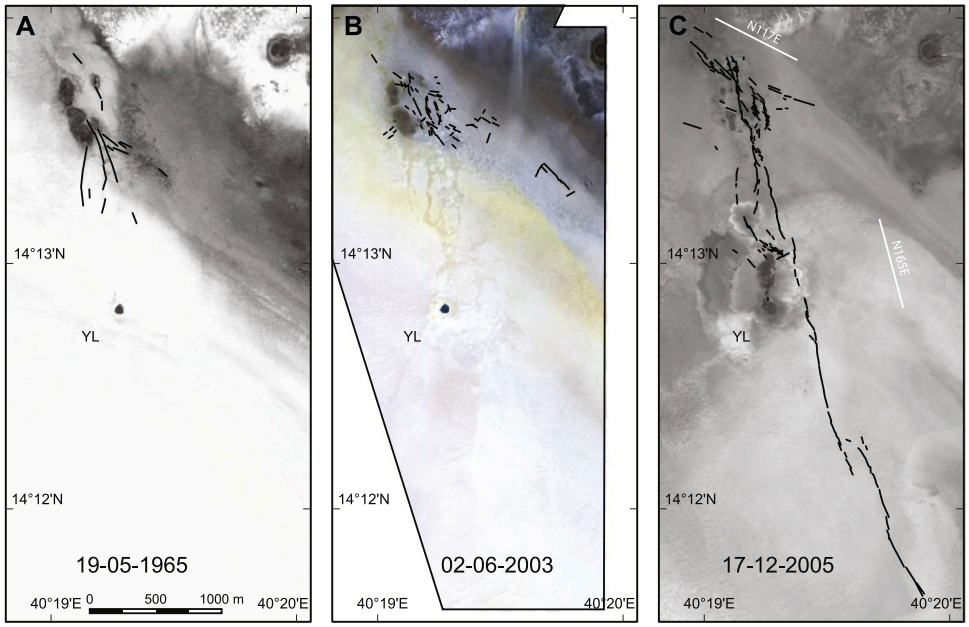

FIGURE 6
Structural evolution of the Yellow Lake Fissure area since 1965. The black lines are fracture lines either exposed at the surface, along which pools are sometimes located, or linear salt plate edge alignments suggestive of deeper tension fracturing or fracturing at subcritical stress. YL: Yellow Lake. **(A)**: fracturing already observed in 1965 by KeyHole 4-A (2.4 m/pixel, image ID); **(B)**: additional fracturing observed in 2003 by Quickbird-2 multispectral (2m/pixel; Gram-Schmidt pansharpened to 0.5 m/pixel). The red, green and blue channels correspond to the bands 4 (0.830 µm), 3 (0.560 µm) and 1 (0.485 µm), respectively; **(C)**: fracturing observed since the first post-YLF high-resolution satellite image, by OrbView-3 (1m/pixel), in 2005. Uninterpreted satellite images are provided in Supplementary Figure S4.

indicating that relay zone fracturing does not pay a critical role in their development.

Segments 6 and 7

These segments are interacting *en échelon* fractures. They are marked on the ground by coalescence of linear 5–10 cm high ridges at the edge of the salt plates located above the fissure, as well as by periodically spaced red circular patches 1 or 2 m in diameter due to native sulphur crystallisation. The relay zone between the two segments shows native sulphur crystallisation on the white salt plates, as well as a few salt bubbles.

4.1.7 Composition and properties of fluids

Water temperature, pH, composition and mineral content of two pools were analysed, and compared to with similar measurements at Yellow Lake (Table 1). Temperature was found to be slightly less than ambient air day temperature (~40°C), and pH moderately acidic. Holwerda and Hutchinson (1968) suggested that the gas in the bubbles of a large brine pool, presumably Yellow Lake, is CO_2. The ambient air temperature is below boiling point, supporting the view that bubbling is a consequence of CO_2 depressuring, perhaps under supercritical conditions (Span and Wagner, 1996) at depth. Brine resurfacing on Mount Dallol itself indicates isotopic exchange with mafic rocks at depth (Gonfiantini et al., 1973). Water composition is close but not similar in the two pools, nor is it identical with the composition of Yellow Lake, suggesting that the fluid source is the same, but its history before reaching the surface differs at the three sites. The identified minerals include halides and chlorides. While most halides and chlorides are found in many possible environments, chloromagnesite is a very rare mineral identified in melt inclusions in unaltered olivines in kimberlites (Golovin et al., 2003) and peridotites (Sharygin et al., 2013). Like at Yellow Lake, chloromagnesite is found with halite and sylvite at fumaroles on Mount Vesuvius (Pelloux, 1927). Finding it in the Yellow Lake may testify to connection with an ultramafic body underneath. Tachyhydrite is another rare mineral because of its tendency to deliquescence. Its detection in Yellow Lake and in the Yellow Pool is made possible by the very high Ca^{2+} concentration. Moors et al. (2023) discuss more results, obtained from various water bodies in the Mount Dallol area.

4.2 Interpretations

4.2.1 Initiation of the Yellow Lake fissure

YLF initiation and evolution can be inferred from the analysis of remote sensing data. Fracturing along the northern segments is apparent in 1965 (Figure 6A), in the form of lineaments which are still observed in 2003 and appear to be at least in part related to Yellow Lake overflow (Figure 6B). However, only on 17 December 2005 is the YLF observed (Figure 6C).

Since 1965, the dominant observed fracture trend is NW-SE to NNW-SSE (Figure 7). In 1965, the YLF trend is clearly dominant (Figure 7A). On 2 June 2003, N117E is the dominant visual trend at the scale of the whole area, and most fracture trends are in the sector NW-SE to N-S. The YLF trend itself, N165E, is visible but does not dominate the trend and length statistics (Figure 7B). On

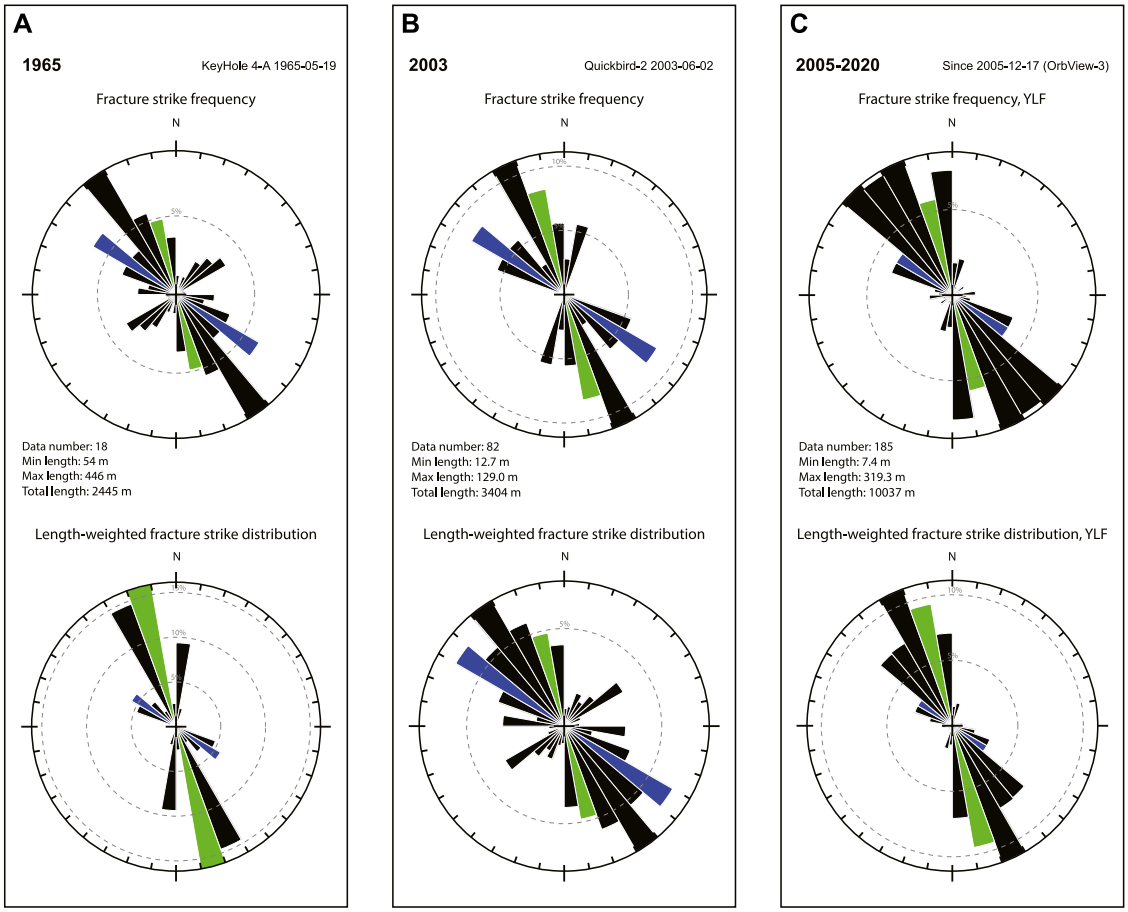

FIGURE 7
Strike analysis for the fractures observed in 1965, the additional fractures observed in 2003, and the fractures observed since 2005 (Figure 6). In the absence of any observed kinematic indicator that would testify to shearing, all the fractures are considered tensile. The upper plots show the frequency of individual fractures. The lower plots show the cumulated frequency of fracture lengths, which better represents the dominant expressed deformation strikes. The green and blue sectors correspond to the mean YLF trend (N167E) and NW-SE fracture trend (N117E), respectively.

17 December 2005 (Figure 7C), the strike frequency and length distribution show a scatter in strike variations between N-S and NW-SE, reflecting the detailed geometry of the fracture network, resulting from the geometry of relay zones and associated propagation patterns. The N117E trend observed in 2003 persists, and intersects the northernmost YLF. Fissure opening is therefore constrained to the time span 2 June 2003—17 December 2005.

The absence of high resolution imagery between June 2003 and December 2005 can be mitigated by time-series analysis of lower resolution imagery during this period in the near-infrared spectral range. Comparison of bands 5 and 7 (30m/pixel) on Landsat-7 images, sharpened by the higher resolution band 8 (15m/pixel), reveals that the composition of the surface changed along the trace of the YLF between 13 October 2004 and 14 November 2004 (Figure 8). The fit to the trace shows that the YLF likely formed within this narrower time interval.

Figure 8 shows that the full length of the YLF was achieved before 14 November 2004. However, the detailed geometry of the segments as seen at the scale of 1m/pixel on 17 December 2005 (Figure 6C) may have been achieved later. There is no spectral evidence of activity of the YLF between 14 November 2004 and 7 April 2005, but narrow resurfacing along the YLF is observed on 10 June 2005, leaving the possibility of renewal of tectonic activity between April and June (Figure 9). The whole study area was flooded by Lake Karum by late April, preventing more precise dating. Hydrothermal activity has been intense in the Yellow Lake area, however, throughout the year 2005 (Supplementary Video S1).

InSAR data analysis indicates that the volcanic crisis that started at Erta 'Ale on 16 January 2017 did not affect the topography in the area of the YLF (Xu et al., 2020). Comparison between satellite imagery before and after the main, January 2017 event (20.11.2016: WorldView-2 vs. 12.02.2017, ASTER), confirms that the fissure system remained unaffected at the surface.

4.2.2 Red salt crust

The red salt crust exposures form together a fragmented elliptic feature (Figure 3). In spite of frequent resurfacing by waters from lake Karum, the water-filled portion of lake Asale, and runoff from the neighbouring mountains, these exposures have been remarkably stable since at least 1965 (Figure 6). Flooding reveals that the red salt crust exposures are subtle topographic highs (Supplementary Figure S5). From direct observations and oral reports, the water column during the floods does usually not exceed 10–20 cm, and numerous

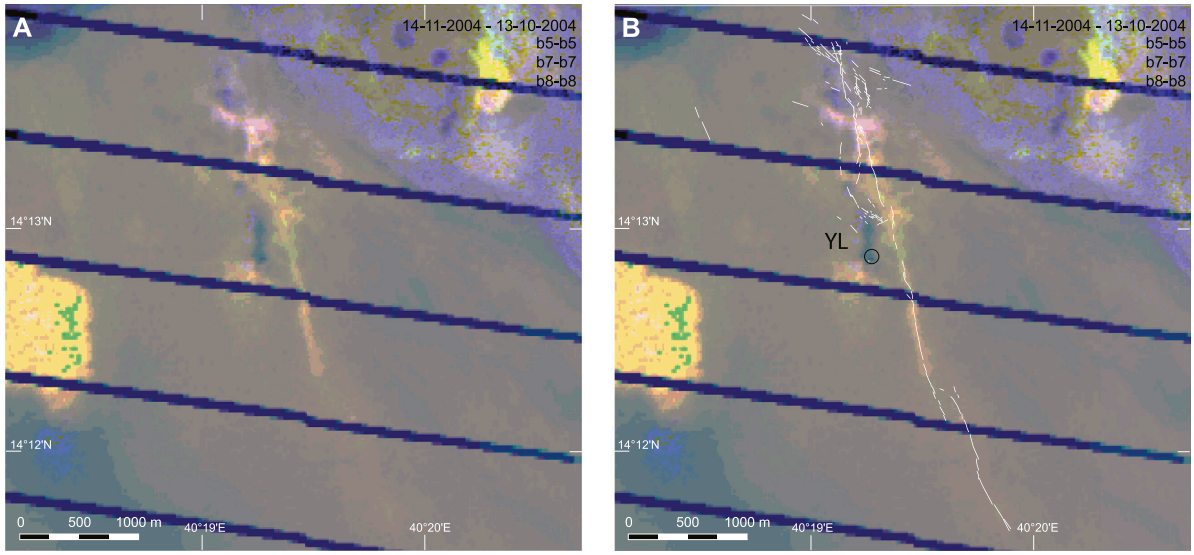

FIGURE 8
Surface change along the YLF trace during fall 2004. The image is a composite colour of Landsat-7 images obtained 14 November 2004 and 13 October 2004. The red, green and blue channels are the difference between bands 5 (1.650 µm, 30 m/pixel), 7 (2.220 µm, 30 m/pixel), and 8 (panchromatic, 15m/pixel), respectively. The YLF structures observed since 17 December 2005 (Orbview-3) are superimposed **(B)** onto the image composite **(A)**.

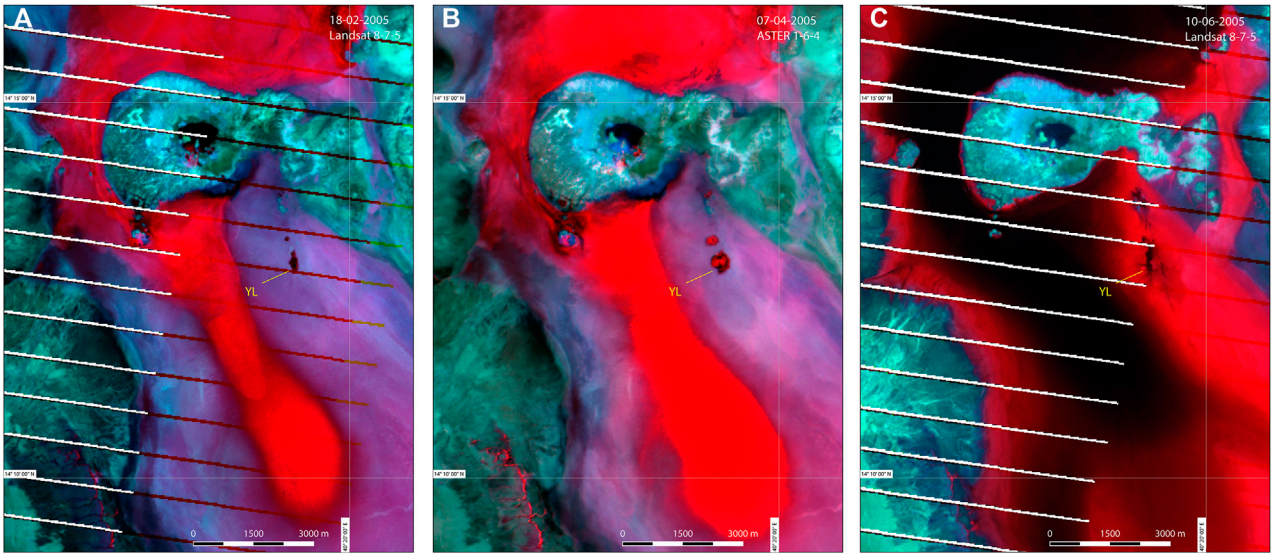

FIGURE 9
Surface change along the YLF trace during winter and spring 2005. The YLF is not much apparent in February **(A)** and March **(B)**, in contrary to June **(C)**, where the YLF trace is well delineated and suggests renewed tectonic activity. Note the changes associated with intense hydrothermal activity focused in the Yellow Lake area. The satellite platforms and composite image band numbers are indicated in the upper right. The band centres for Landsat data are located at 0.710 µm (band 8, red), 2.220 µm (band 7, green), and 1.650 µm (band 5, blue). The band centres for ASTER data are located at 0.650 µm (band 1, red), 2.205 µm (band 6, green), and 1.650 µm (band 4, blue).

Landsat-7, Landsat-8, and ASTER images show that flooding very rarely attains the top of the red salt exposures. Topographic analysis of the data from the UAV-borne stereophotogrammetric survey confirms that the red salt crust is a local high, perhaps up to 50 cm with respect to the surrounding salt flat (Figure 10). The YLF itself is not significantly more elevated than its surroundings.

The red salt crust exposures are older than any available high-resolution satellite image. In spite of a resolution of 28 m only, a 1962 KeyHole-5 mission image distinctly shows that they were already present in 1962. The origin may be either a mud flow, or doming above a diapir. Several diapirs are exposed east of the YLF area (Figure 1).

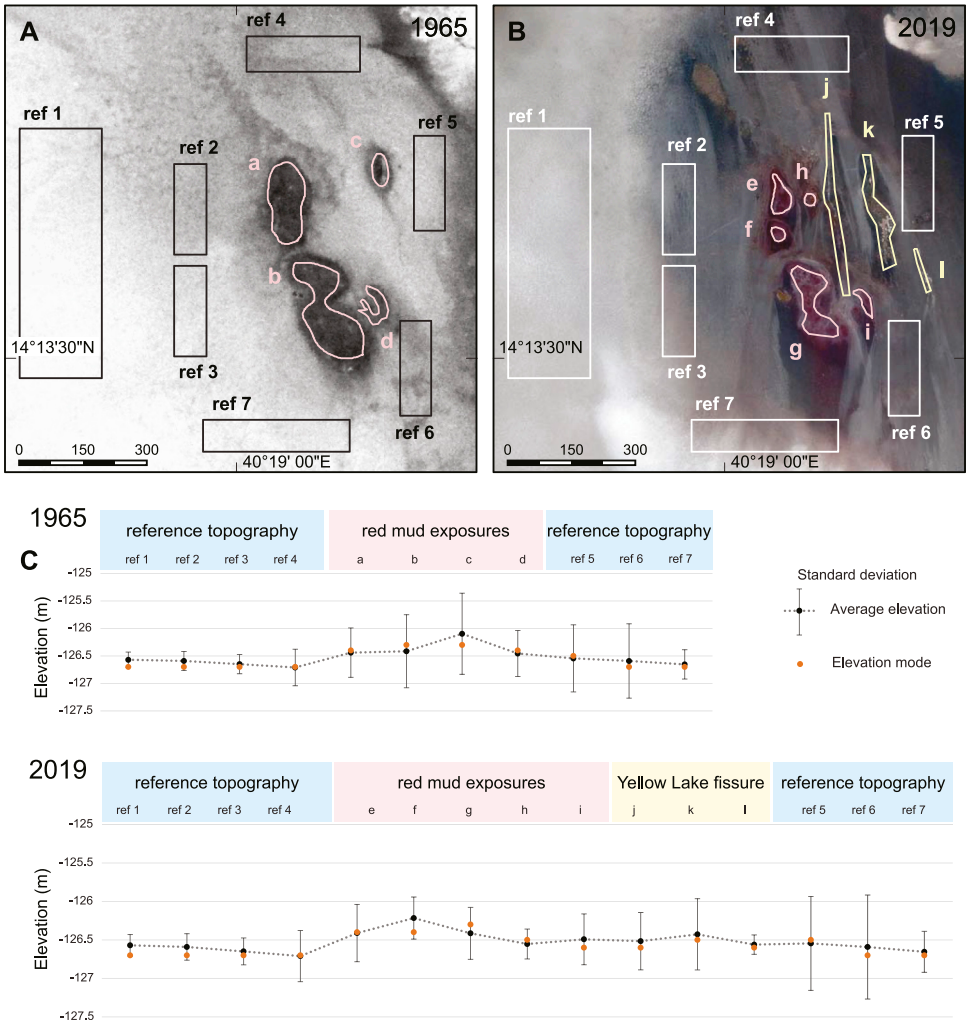

FIGURE 10
(A) Red salt crust surface areas (a to d) and reference surface areas in the surrounding salt flat (ref 1 to ref 7) used for topographic analysis. KeyHole-4A, 2.4 m/pixel, 1965-05-19; **(B)** Red salt crust surface areas (e to i), YLF surface areas (j to l), and reference areas in the surrounding salt flat (ref 1 to ref 7) used for topographic analysis. Pleiades 1B, 2 m/pixel with Gram-Schmidt sharpening using panchromatic band at 0.5 m/pixel, 2019-02-26; **(C)** Topographic analysis.

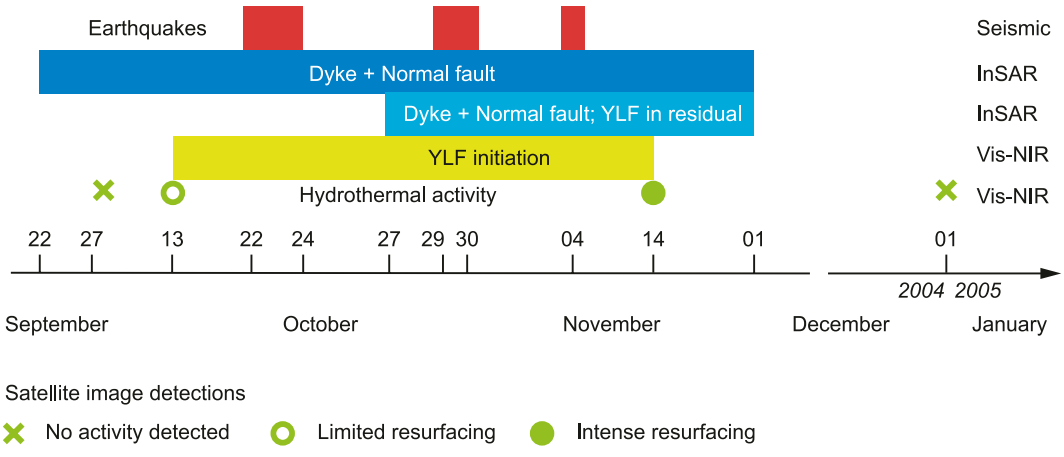

FIGURE 11
Chronology of seismic activity, dyke emplacement, and tectonic and hydrothermal activity in the YLF area in 2004 and 2005. Data from seismic stations and InSAR modelling are as in Nobile et al. (2012). Other information is from this work.

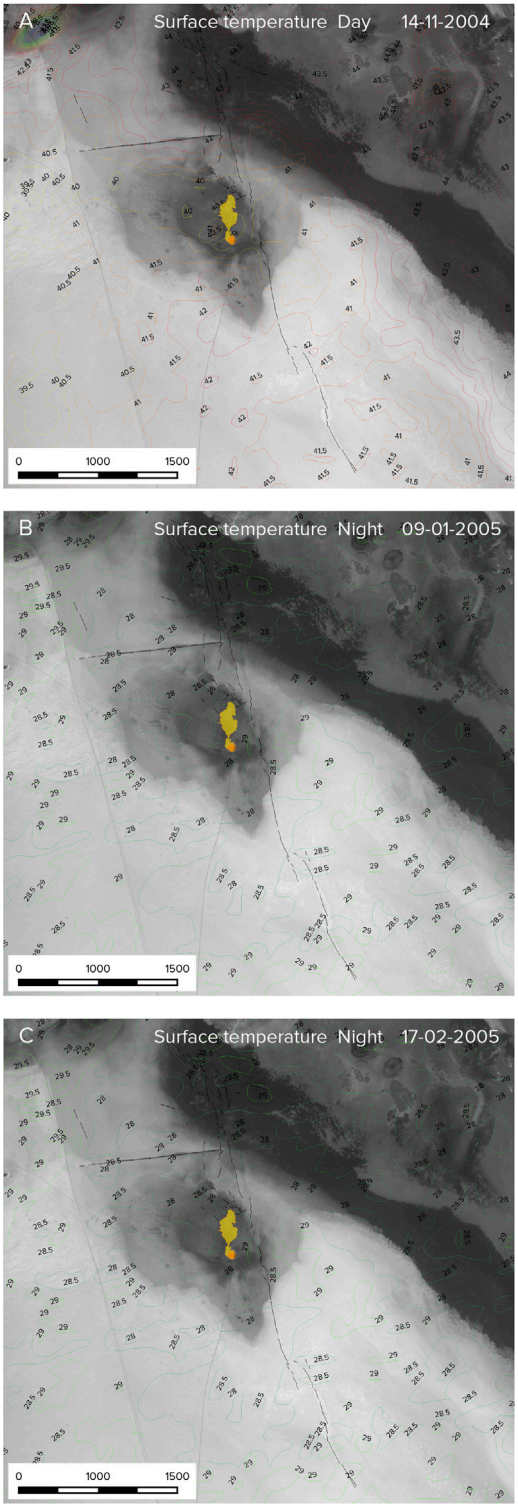

FIGURE 12
Terra/ASTER surface kinetic temperatures during YLF formation (2004–2005) from Terra/ASTER. The kinetic temperatures are made available by the NASA EOSDIS Land Processes Distributed Active Archive Center (LP DAAC) as product AST_08. Kinetic temperature is provided here in °C as contours with interval 0.5°C for the three ASTER datasets covering the initiation time of the Yellow Lake Fissure. The background image is from Pleiades-1B, 24-01-2019. Black lines: Yellow Lake Fissure (YLF) segments; Orange circle: Yellow. There is no thermal anomaly observed that could be associated with (*Continued*)

FIGURE 12 (Continued)
either the YLF nor Yellow Lake, whether during day-time **(A)** or night-time **(B, C)**. Landsat-7 monitoring (Supplementary Video S1) reveals that the temperatures on **(C)** correspond to a Yellow-Lake focused hydrothermal crisis, indicating that the hydrothermal fluid flow was at low (ambient) temperature, and resulted from fluid overpressure more than heating. The product IDs are provided in Supplementary Table S2. The data used here are correspond to AST_08 version 3: https://lpdaac.usgs.gov/products/ast_08v003/.

4.2.3 Hydrothermal activity at Yellow Lake and YLF

A review of satellite images obtained in 2004 and 2005 makes it possible to reconstruct the evolution of hydrothermal activity since YLF formation (Supplementary Video S1). Hydrothermal activity appears on multispectral imagery on 14 November 2004 (Figure 8). As soon as the YLF was formed, hydrothermal activity occurred north of Yellow Lake. The dark deposits which are visible north of Yellow Lake on Figure 8 correspond to hydrothermal activity that was ongoing between October and November 2004. This activity is clear on the Supplementary Video S1, which further shows that it resumed in the second half of January 2005, and lasted until early April 2005 at least. The area was then fully flooded, with the possible exception of the two highest points of the red salt crust. There is evidence of continuing hydrothermal activity north of Yellow Lake between July and December 2005 (Figure 11).

The situation is more accurately known in mid-December 2005 thanks to availability of high-resolution imagery. The dark deposits north of Yellow Lake on Figure 6 are connected to Yellow Lake, suggesting that they were formed during a Yellow Lake overflow event (brown on Figure 3). They are surrounded by light-edged salt lobes marking the maximum extent of the flooding. It is apparent from the Supplementary Video S1 that the lobes include material emitted by a 300 m long, N-S oriented fissure starting at Yellow Lake (dashed black line on Figure 3), and another, 100 m long NNW-SSE oriented fissure a few hundred meters in the North. The N-S was not seen in the field in 2018 and 2019, whereas the NNW-SSE-oriented fissure could be, through the preferred orientation of salt plate fractures, and to associated subsurface bubbling and venting.

4.2.4 Pressure-driven, low-temperature hydrothermal flow

Whether magmatic heat was significant in the process of YLF development may be evaluated by the temperature of the fluids at the surface when the fissure open. The temperature of the fluids that were first ejected from the hydrothermal fissure, and led to resurfacing along its trace is investigated using thermal data obtained by ASTER (Figure 12) and MODIS (Figure 13). ASTER surface temperatures are available for 14-11-2004 during daytime, just after YLF initiation. They are also available on 09-01-2005 and 17-02-2005 at night time, at the beginning of a hydrothermal crisis centred at the Yellow Lake area. MODIS daily daytime and night time temperatures are available at a resolution of 1 km. None of these datasets show evidence of anomalous surface temperatures in this time span, suggesting that the fluids that accompanied YLF opening during fall 2004 and those of the subsequent hydrothermal crisis did not advect significant thermal energy to the surface. Similar fluid temperatures were measured in 2018 (Table 1).

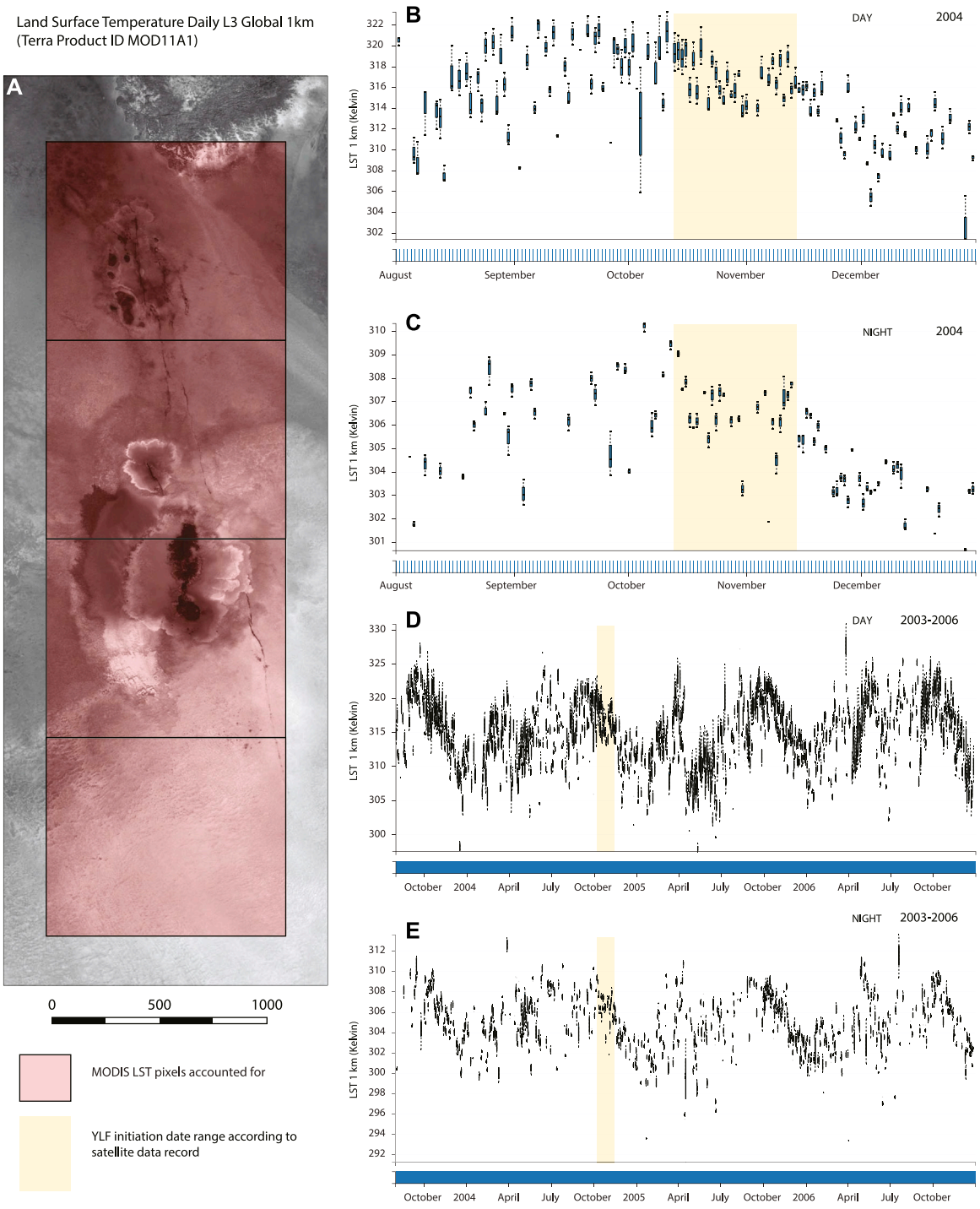

FIGURE 13
Terra/MODIS surface temperature during YLF formation (2004–2005). The figure synthesizes the gridded, 1 km/pixel daily MODIS Land Surface Temperature (Wan et al., 2015) in the YLF area **(A)** between August and December 2004 at day time **(B)** and night time **(C)**, and between August 2003 and December 2006 at day time **(D)** and night time **(E)**. **(B, C)** do not show any anomalous surface temperature compared to the weeks before and after YLF initiation. **(D, E)** show that surface temperatures followed similar cycles in the time span 2003–2006.

Although not measured, the temperature of White Lake, which was the most active bubbling body during the 2019 field visit, was also similar to ambient air, suggesting that bubbling was only due to exsolution caused by reducing pressure in the rising fluids.

In contrast, near Black Mountain and Mount Dallol, hot springs having temperatures as high as 130°C had been measured in the 1920's (as reported by Holwerda and Hutchinson, 1968; Talbot, 2008). The pond located at the northern tip of Black Mountain, visited in January 2018, was found to be at ambient air temperature as well.

5 Discussion

5.1 Dyke emplacement and YLF opening

The uncertainty on the initiation time of the YLF, constrained to the period between October 13 and 14 November 2004 encompasses the whole period of Black Mountain dyke injection inferred from the seismic record, i.e., October 22–November 4 (Nobile et al., 2012). Independently, InSAR modelling constrains dyke intrusion to two events, the main one between October 22 and October 26, and a minor event between October 27 and 1 December 2004. Figure 11 summarizes the time constraints of tectonic and hydrothermal activity at the YLF, compared to the timing of seismic ruptures recorded at nearby seismic stations and dyke emplacement inferred from InSAR modelling.

The model inferred from the InSAR ground deformation calculations for the period 22/09/2004–01/12/2004 includes the Black Mountain dyke, as well as a blind normal fault located west of the dyke (Nobile et al., 2012). The fault is parallel to the dyke and to the Danakil rift margin, where seismic profiles indeed show rift-parallel border faults (Figure 3), one of which might have been reactivated by dyke emplacement (Bastow et al., 2018). The model residual does not show any influence of YLF development on ground deformation during this period. However, when the narrower, October 27—December 1st time span is considered, during which 13% of the dyke was injected (Nobile et al., 2012), the InSAR model residual appears consistent with ground displacement along the YLF (Supplementary Figure S6). Combining information from satellite image monitoring and InSAR modelling, it appears likely that the YLF formed between October 27 and 14 November 2004, consistent with the timing of second magma injection in the Black Mountain dyke, strongly suggesting a genetic link.

5.2 Hydrothermal activity in the YLF area in response to a Dallol sill

The red salt crust exposures have been observed for several decades. Bubbling at Yellow Lake has also been reported since Holwerda and Hutchinson (1968), testifying to permanently pressured groundwater underneath. White Lake, the largest water body in the YLF area, was vigorously bubbling during the 2019 field campaign (Figure 5A), and KeyHole imagery indicates that it is a long-living lake as well, developed from the merging of two smaller lakes visible in 1965 (Figure 6). Evidence of groundwater release, and therefore pressuring underneath, exists at these sites for as long as data are available. It requires a degassing source at depth much before the 2004 Black Mountain dyke intruded the crust. This source may be a magmatic intrusion underneath, old enough for the temperature of the hydrothermal fluids to have cooled to the ambient temperature at surface.

We follow the interpretation of a less than 6,000 years-old sill intruding the salt formations, as advocated by López-García et al. (2020), for the following reasons. First, Holwerda and Hutchinson (1968) mentioned the existence of rare altered basalt fragments in salt dykes on Mount Dallol. Dolerite enclaves were indeed fund in salt dykes on the western slope of Mount Dallol during our 2019 campaign (Supplementary Figure S7), strengthening the hypothesis of a dyke or sill underneath. Secondly, a N-S trending seismic profile acquired for Yara Dallol BV north of Mount Dallol shows that the evaporite beds are increasingly uplifted toward Mount Dallol (Supplementary Figure S8; Environmental Resources Management Southern Africa (Pty) Ltd., 2014), which might be an effect of layer upwarping at the contact of the intruding sill (Galland and Scheibert, 2013).

Sill development from a dyke, as suggested by Warren (2015) at Mount Dallol, is mechanically well understood (e.g., Gressier et al., 2010). In particular, the effect of the specific rheology of salts especially hydrated, on this evolution, has been investigated (e.g., Schofield et al., 2014). The Houston Formation offers a range of hydrated mineral-rich layers (mainly, from bottom to top, kainite, carnallite, bischofite, and carnallite; Rauche van der Klauw, 2015), the mechanical strength of which is small (Urai et al., 1986; 2017; Rowan et al., 2019) and easily further decreased by decomposition and melting at low temperature. The melting temperature of carnallite and bischofite, 110°C–120°C (Warren, 2016), may allow them to melt ahead of a propagating intrusion even before their contact, depending on the combination of reaction kinetics, ambient thermal diffusivity, and intrusion propagation speed. The resulting brines would recrystallize further away around the intrusion as new, more competent, anhydrous or less hydrated minerals (Schofield et al., 2014). The strata of the Houston formation containing hydrous minerals is capped with layers exclusively composed of anhydrous minerals of higher mechanical strength (halite, anhydrite, and sylvite; Rauche and van der Klauw, 2015). These layers would overlie the intruded sill.

If Mount Dallol indeed uplifted in response to sill intrusion, the dimensions of the sill (hereafter called the Dallol sill) should be large enough to uplift Dallol by tens of metres, from which a complex intrusion geometry would be expected; in particular, the Dallol sill may have extended to adjacent areas as thinner, secondary magma sheets connected to the main intrusion. It would have propagated far enough toward Yellow Lake to continue nowadays to pressure groundwater in this area, fed by the fluid-saturated sediments (Talbot, 2008) between the sill and the surface.

From drilling core data, Rauche and van der Klauw (2015) extrapolated the depth of the top of the Marker Beds to 350–400 m south of Yellow Lake (Supplementary Figure S9). The Houston Formation is shallower at Yellow Lake and the southern YLF than in most other place of lake Asale south of Dallol in areas where drilling cores are available. This may be the reason why hydrothermal activity visible at the surface south of Dallol is concentrated in the YLF area instead of anywhere else.

5.3 Integrating hydrothermal and tectonic activity at the YLF

The following two-stage evolution is an attempt to reconcile the long-lasting hydrothermal activity in the YLF area and the recent (2004) opening of the fissure (Figure 14).

1) The Dallol sill, then not yet cooled (López-García et al., 2020), propagated in the Potash Beds of the Houston Formation (Warren, 2015). This stratigraphic level is particularly shallow, and the branch of the propagated sill would probably be closer to the surface in the YLF area than in many other areas south of Mount Dallol (Figure 14A),

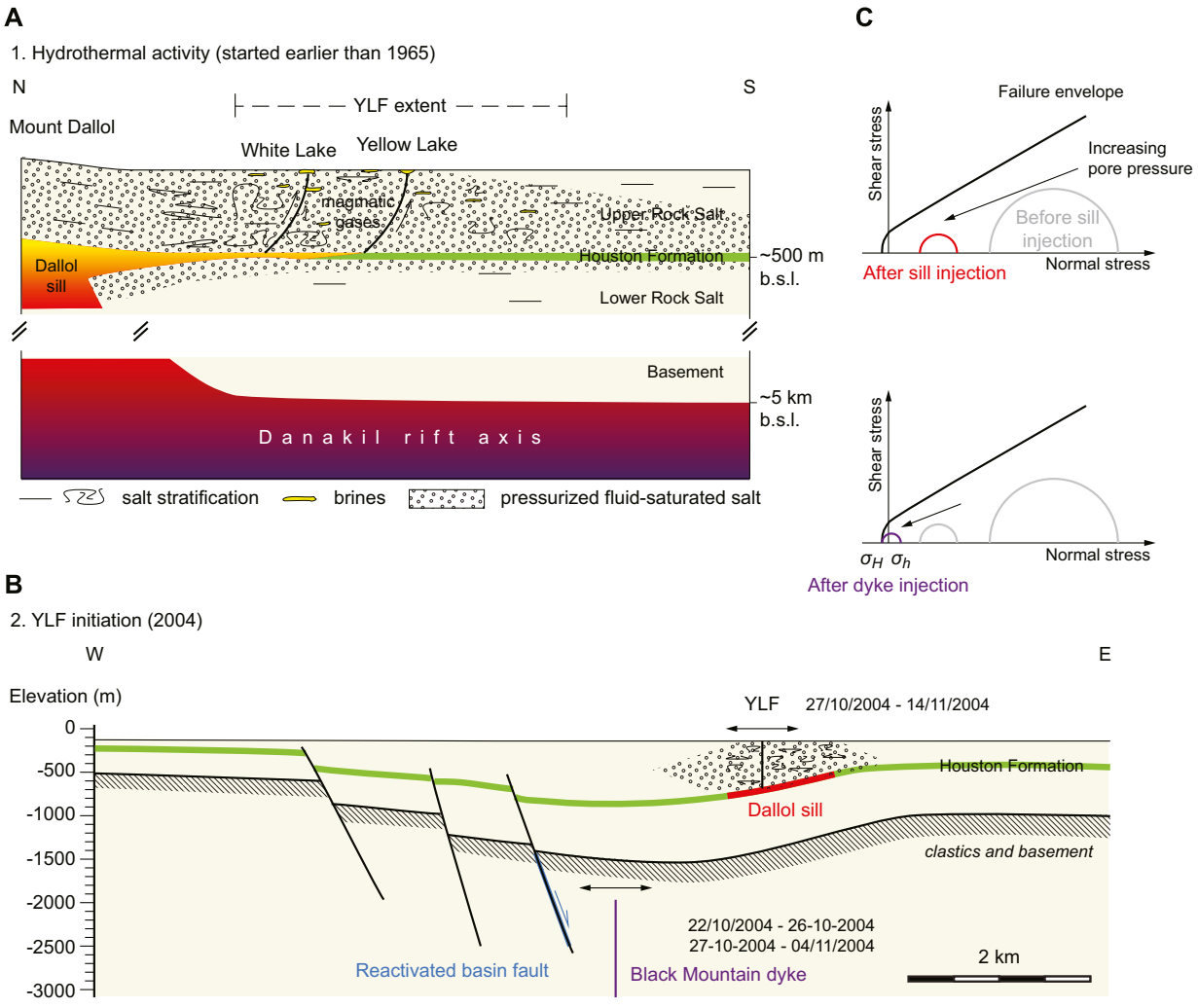

FIGURE 14
Interpreted hydrothermal and structural evolution of the Yellow Lake Fissure area. The Houston Formation depth variations are taken from Rauche and van der Klauw (2015). Vertical exaggeration 1:1. **(A)** Hydrothermal stage. Hydrothermal activity at Yellow Lake and the future YLF is driven by overpressured water-saturated salt body over the Houston Formation-intruded Dallol sill. Hydrothermal activity occurs at Yellow Lake, White Lake and pools. Sill intrusion occurs at the Houston Formation (Warren, 2015; López-García et al., 2020), which here is at a depth of ~400 m below the surface (Rauche and van der Klauw, 2015). The Dallol sill is here interpreted to have initiated from a source in the rift axis, at a depth similar to the maximum depth of the deepest dyke that intruded the Erta 'Ale volcano in 2017 (Moore et al., 2019). **(B)** Tectonic stage. Black Mountain dyke emplacement occurred in two steps, before and after 27 October 2004. Both steps were accompanied by normal faulting (Nobile et al., 2012). Here the reactivated normal fault is interpreted from the contour map of the Marker Beds, on top of the Houston Formation (Supplementary Figure S9), and approximately corresponds to the fault location predicted by Nobile et al. The portion of the fault reactivated during the dyke injection is in blue. The YLF would have formed following the second dyke injection event, in the part of the evaporites weakened by the overpressured saturated salts. This would accommodate the extension in the evaporites overlying the area of extension within bedrock due the dyke intrusion and fault reactivation. The profile end points used are (14.1785°N 40.2426°E) and (14.2113°N 40.3480°E). **(C)** Formation of YLF by tension failure with increasing pore pressure. σ_H is the maximum horizontal principal stress and σ_h the minimum horizontal principal stress.

triggering more visible hydrothermal activity at surface in the fluid-saturated evaporite basin. This situation would have started earlier than the satellite image data record. Hydrothermal activity would also explain the deggasing of White Lake, and be involved in the formation of hydrothermal pools. López-García et al. (2020) already suggested that Yellow Lake hydrothermal activity is an effect of Dallol sill degassing.

2) Propagation of the Black Mountain dyke in 2004 triggered opening of the YLF (Figure 14B). The whole crust is in extensional regime, being at a diverging plate boundary. In response to the far-field stress, crustal dilation at depth needs to be balanced by tectonic stretching at shallower depth and the surface (e.g., Forslund and Gudmundsson, 1991). The YLF would therefore contribute to release the tensional stress of the plate boundary at the surface, released in depth by dyke dilation and blind reactivation (Rubin and Pollard, 1988) of one of the rift basin normal fault (Nobile et al., 2012). This interpretation implies that the residual of the interferometric model of Nobile et al. (2012) between 27/10/2004 and 01/12/2004 includes the YLF signature, as shown on Supplementary Figure S6.

In the second stage, the YLF initiates at a site where the salt pile was close to failure (Figure 14C, top). Continuous groundwater pressuring in the YLF area (Figure 14C, bottom), or groundwater pressuring in response to sealing by some salt levels, brought the stress deviator close to rupture, and promoted tensile fracturing (Tingay et al., 2003; Mourgues et al., 2011). The distribution of the dyke, the normal fault and YLF is actually close to models of host rock fractured around intruding dykes in extensional environment or with free lateral boundary conditions. For instance, Rubin and Pollard (1988) and Abdelmalak et al. (2012) found that emplacement of vertical dykes at depth (i.e., dykes whose upper tip does not rotate) promotes normal faulting on the dyke upper lateral side, and tension fracturing at a higher level and to the surface. Physical models that include mechanical layering and expandable lateral boundary conditions, both particularly adapted to the lake Asale conditions, yielded similar conclusions (Mastin and Pollard, 1988). Following these results, formation of the YLF may be viewed as an anticipated consequence of the intrusion of the Black Mountain dyke.

It is also possible that a proto-YLF already existed in the past, although not observed on satellite imagery before 2004. For instance, Figures 6A, B shows linear patterns in 1965 and 2003 which be interpreted as surface flows, but their linear pattern as well as the inability of the seasonal floods to remove them from the surface between 1965 and 2003 favours a tectonic instead of a surficial origin.

5.4 Implications for intrusive and hydrothermal activities at mid-ocean ridges

In the study area, the Dallol sill intrusion propagating in one of the weakest evaporite levels generates, on the one hand, long-lasting, diffuse hydrothermal activity in the evaporites, and on the other hand, mechanical changes in these evaporites that help focus further deformation. Dyke injection then provides the deviatoric stress increase that triggers directional, fissure-driven, hydrothermal activity. Does such a magmatic-tectonic-evaporitic-hydrothermal system exist in other extensional environments?

The scale of the processes studied here goes actually beyond the resolution that most data from past or recent offshore cruises can reveal. Not surprisingly, therefore, the proposed mechanism has not been described in the literature yet. It may, however, be operative at slow and ultraslow spreading centres.

One such extensional system may be the slow-spreading Red Sea spreading centre. The Danakil depression is an incipient spreading ridge connected to the Red Sea. Using InSAR data, Moore et al. (2019) interpret stacked large melt lenses in the upper crust feeding shallow magma chambers in the Erta ʿAle volcano, which sits in the Danakil depression 25 km south of the YLF. North of the Danakil depression, the Red Sea seafloor consists of a volcanic, oceanic crust (Augustin et al., 2021; Delaunay et al., 2023) widely covered by evaporites (Mitchell et al., 2010; Augustin et al., 2014; Feldens and Mitchell, 2015; Delaunay et al., 2023). Moreover, seismic profiles across the central Red Sea by Sang et al. (2023) show disturbances in the evaporite sequence which may be interpreted as interstratified sills. The conditions for the interplay between evaporites, dyke and sill intrusions, and hydrothermal circulation as discussed in the present work may therefore plausibly extend from the Erta Ale to the whole Red Sea.

Another possibly relevant slow-spreading ridge may be the ridge entering the Gulf of California, separating Baja California from North America, where the seafloor of some segments is also partly covered by evaporites, deposited on top of the volcanic basement (Miller and Lizzaralde, 2013; Helenes et al., 2020). For instance, at the axis of the Pescadero Basin, Ramírez-Zerpa et al. (2022) showed from seismic reflection that hydrothermal vents developed on sediments as a result of the intrusion of sills underneath along the rift axis. Vent activity is explained by advective flow in the possibly saturated sediments above the sills. This interpretation is close to the interpretation of hydrothermal activity at White Lake and Yellow Lake in the YLF area (Figure 14A).

Fracture-controlled hydrothermal activity in response to dyke emplacement as in Figure 14B may still be considered as a viable mechanism for linear hydrothermal vents even in the absence of salts, because the Mastin and Pollard (1988) dyke emplacement model which it is inspired of does not specifically require evaporites. For instance, McDermott et al. (2022) noted that in addition to dyke-controlled hydrothermal vents at the East Pacific Rise axis, off-axis fault-controlled hydrothermal vents also formed at a distance of ~750 m to the ridge axis. This distance is smaller than, but of the same order of, the 2 km measured in the Dallol area (Figure 14B). Although the East Pacific Rise is a fast-spreading ridge, involving significantly different relationships between tectonics and magmatism from those prevailing in the Dallol area, mechanical relationships between dyking and fracturing might also follow the Mastin and Pollard (1988) model, providing a potential explanation for the 750 m offset.

Generally, sill and hydrothermal activity offset with respect to the active spreading axis have been reported from ridges at all spreading rates. On the Mid-Atlantic Ridge, the Trans-Atlantic Geotraverse (TAG) hydrothermal field was shown from bathymetry, seismic refraction data, and earthquake distribution, to be offset from the axial magma chamber in relation to a detachment fault system (deMartin et al., 2007; Szitkar et al., 2019), as also observed on numerous oceanic core complexes of the slow and ultraslow poorly magmatic spreading centres (e.g., Dyment et al., 2018; Zhou et al., 2022). At the intermediate Juan de Fuca ridge, where the crust builds by dyking and sea-floor eruptions, seismic reflection profiles reveal the presence of sills offset from the axial magma centre. Hydrothermal vents are also offset from the spreading axis (Canales et al., 2009). Higher-resolution bathymetry and geophysics in such areas may reveal in the future whether relationships between dyke and sill emplacement on the one hand, and hydrothermal activity on the other hand, such as proposed in this work is frequent at oceanic spreading centres.

6 Conclusion

This work provides the first description and analysis of a 15 years old fissure system located in northern Afar at the boundary between the Nubian plate and the Danakil microplate, that we named the Yellow Lake Fissure. We mapped and characterised the geologic activity of the

fissure system, emphasizing the diversity of its surface morphology. Using spaceborne data, we showed that its initiation was coeval with emplacement of the Black Mountain dyke (as we named the dyke that intruded the crust below Lake Asale in 2004). Hydrothermal activity was found to be lasting for several decades, whereas the fissure itself formed in 2004. We proposed a two-stage scenario to explain the formation and evolution of this hydrothermal-tectonic system, involving igneous activity in Mount Dallol and associated secondary magma bodies, the dyke which intruded the crust in 2004, and the local groundwater conditions.

The western arm of the Red Sea spreading centre enters the northern Afar in the Gulf of Zula. The Yellow Lake Fissure belongs to this incipient plate boundary. Although modest, a few kilometres in length, it appears to be the only currently active fissure of northern Afar, and its dynamics is likely related to that of the Red Sea spreading centre. The fissure provides unique constraints on the magmatic, tectonic, and hydrothermal processes that affect a rift in transition from continent to ocean.

Data availability statement

The original contributions presented in the study are included in the article/Supplementary Material, further inquiries can be directed to the corresponding author.

Author contributions

DM: Project management; funding; field data collection and analysis; satellite data analysis, manuscript writing. EH: Field data collection and analysis; manuscript writing. JD: Data analysis; manuscript writing. PA: Funding; field data collection; digital terrain model generation; HM: Field data collection and sample analysis; manuscript writing; MD, HC: field data collection; data analysis. All authors contributed to the article and approved the submitted version.

Funding

Field work was funded by Europlanet 2020 RI, and laboratory work by DM by the EXOMHYDR project and a joint fellowship of the Polish Academy of Sciences and CNRS at Institut de physique du globe de Paris. Europlanet 2020 RI has received funding from the European Union's Horizon 2020 research and innovation program under grant agreement No. 654208. The EXOMHYDR project is carried out within the TEAM program of the Foundation for Polish Science co-financed by the European Union under the European Regional Development Fund.

Acknowledgments

Structural analysis shown in Figure 8 was conducted using SG2PS (Sasvári and Baharev, 2014). Harald Hansen, Henok Tsegaye, and the Yara Dallol B. V. field camp staff are thanked for help in field logistics, and Benjamin Van Wyk De Vries and Viktor Vereb for enjoyable joint field work at the Dallol salt dykes. We thank two reviewers and Neil Mitchell for careful reviews and suggestions which enriched and broadened the discussion. The identification of potential sills in the Sang et al. (2023) seismic dataset is to be credited to Neil Mitchell.

Conflict of interest

The authors declare that the research was conducted in the absence of any commercial or financial relationships that could be construed as a potential conflict of interest.

Publisher's note

Supplementary material

The Supplementary Material for this article can be found online at: https://www.frontiersin.org/articles/10.3389/feart.2023.1250702/full#supplementary-material

References

Abdelmalak, M. M., Mourgues, R., Galland, O., and Bureau, D. (2012). Fracture mode analysis and related surface deformation during dyke intrusion: results from 2D experimental modelling. *Earth Planet. Sci. Lett.* 359 (360), 93–105. doi:10.1016/j.epsl.2012.10.008

Albino, F., and Biggs, J. (2021). Magmatic processes in the East African rift system: insights from a 2015–2020 sentinel-1 InSAR survey. *Geochem. Geophys. Geosystems* 22, e2020GC009488. doi:10.1029/2020GC009488

Anderson, M., and Goode, T. C. (2017). "Appropriate catchment management can improve the profitability of a mine: a case study from Dallol, Ethiopia," in *IMWA proceedings, mine water and circular economy (vol I)*. Editors C. Wolkersdorfer, L. Sartz, M. Sillanpää, and A. Häkkinen (Lappeenranta: Finland), 633–641.

Augustin, N., Devey, C. W., van der Zwan, F. M., Feldens, P., Tominaga, M., Bantan, R., et al. (2014). The rifting to spreading transition in the Red Sea. *Earth Planet. Sci. Lett.* 395, 217–230. doi:10.1016/j.epsl.2014.03.047

Augustin, N., van der Zwan, F. M., Devey, C. W., and Brandsdóttir, B. (2021). 13 million years of seafloor spreading throughout the Red Sea basin. *Nat. Comms* 12, 2427. doi:10.1038/s41467-021-22586-2

Barnie, T. D., Keir, D., Hamling, I., Hofman, B., Belachew, M., Carn, S., et al. (2016b). "A multidisciplinary study of final episode of the Manda Hararo dyke sequence, Ethiopia, and implications for trends in volcanism during the rifting cycle," in *Magmatic rifting and active volcanism 420*. Editors T. J. Wright, A. Ayele, D. J. Ferguson, T. Kidane, and C. Vye-Brown (London: Geol. Soc. London, Sp. Publ), 149–163. doi:10.1144/SP420.6

Barnie, T. D., Oppenheimer, C., and Pagli, C. (2016a). *Does the lava lake of Erta 'Ale volcano respond to regional magmatic and tectonic events? An investigation using Earth Observation data: geological Society Special Publication, v. 420*. London: Geological Society Special Publication, 181–208. doi:10.1144/SP420.15

Belachew, M., Ebinger, C., Coté, D., Keir, D., Rowland, J. V., Hamond, J. O. S., et al. (2014). Comparison of dike intrusions in an incipient seafloor-spreading segment in

Afar, Ethiopia: seismicity perspectives. *J. Geophys. Res.* 116, B06405. doi:10.1029/2010JB007908

Bosworth, W., Huchon, P., and McClay, K. (2005). The Red Sea and Gulf of aden basins. *J. Afr. Earth Sci.* 43, 334–378. doi:10.1016/j.jafrearsci.2005.07.020

Canales, J. P., Nedimović, M. R., Kent, G. M., Carbotte, S. M., and Detrick, R. S. (2009). Seismic reflection images of a near-axis melt sill within the lower crust at the Juan de Fuca ridge. *Nature* 460, 89–93. doi:10.1038/nature08095

Delaunay, A., Baby, G., Fedorik, J., Afifi, A. M., Tapponnier, P., and Dyment, J. (2023). Structure and morphology of the Red Sea, from the mid-ocean ridge to the ocean-continent boundary. *Tectonophysics* 849, 229728. doi:10.1016/j.tecto.2023.229728

deMartin, B. J., Son, R. A., Canales, J. P., and Humphris, S. E. (2007). Kinematics and geometry of active detachment faulting beneath the Trans-Atlantic Geotraverse (TAG) hydrothermal field on the Mid-Atlantic Ridge. *Geology* 35, 711–714. doi:10.1130/G23718A.1

Dyment, J., Szitkar, F., and Levaillant, D. (2018). Ridge propagation, oceanic core complexes, and ultramafic-hosted hydrothermalism at Rainbow (MAR 36°N): insights from a multi-scale magnetic exploration. *Earth Planet. Sci. Lett.* 502, 23–31. doi:10.1016/j.epsl.2018.08.054

Eagles, G., Gloaguen, R., and Ebinger, C. (2002). Kinematics of the Danakil microplate. *Earth Planet. Sci. Lett.* 203, 607–620. doi:10.1016/S0012-821X(02)00916-0

Ebinger, C., Ayele, A., Keir, D., Rowland, J., Yirgu, G., Wright, T., et al. (2010). Length and timescales of rift faulting and magma intrusion: the Afar rifting cycle from 2005 to present. *Annu. Rev. Earth Planet. Sci.* 38, 439–466. doi:10.1146/annurev-earth-040809-152333

Environmental Resources Management Southern Africa (Pty) Ltd (2014) *Final scoping report for the Yara Dallol Potash environmental and social impact assessment study. Report 0224244*. Addis Ababa: Yara Dallol BV.

Farr, T. G., Rosen, P. A., Caro, E., Crippen, R., Duren, R., Hensley, S., et al. (2007) The Shuttle radar topography mission. *Rev. Geophys* 45, RG2004. doi:10.1029/2005RG000183

Feldens, P., and Mitchell, N. C. (2015) "Salt flows in the central Red Sea" in *The Red Sea* N. M. A. Rasul and I. C. F. Stewart, Cham; Springer. doi:10.1007/978-3-662-45201-1_12

Forslund, T., and Gudmundsson, A. (1991). Crustal spreading due to dikes and faults in southwest Iceland. *J. Struct. Geol.* 13, 443–457. doi:10.1016/0191-8141(91)90017-D

Franzson, H., Helgadóttir, H. M., and Óskarsson, F. (2015). "Surface exploration and first conceptual model of the Dallol geothermal area, Northern Afar, Ethiopia," in Proc. World Geotherm. Congress 2015, 11043, Australia-New Zealand, 16-24 April 2015, 11.

Galland, O., and Scheibert, J. (2013). Analytical model of surface uplift above axisymmetric flat-lying magma intrusions: implications for sill emplacement and geodesy. *J. Volcanol. Geotherm. Res.* 253, 114–130. doi:10.1016/j.jvolgeores.2012.12.006

Golovin, A., Sharygin, V., Pokhilenko, N., Mal'kovets, V., and Sobolev, N. (2003). Secondary melt inclusions in olivine from unaltered kimberlites of the Udachnaya-Eastern pipe. *Yakutia. Int. Kimberl. Conf. Ext. Abstr.* 8. doi:10.29173/ikc3141

Gonfiantini, R., Borsi, S., Ferrara, G., and Panichi, C. (1973). Isotopic composition of waters from the Danakil depression (Ethiopia). *Earth Planet. Sci. Lett.* 18, 13–21. doi:10.1016/0012-821X(73)90028-9

Gressier, J. B., Mourgues, R., Bodet, L., Matthieu, J. Y., Galland, O., and Cobbold, P. (2010). Control of pore fluid pressure on depth of emplacement of magmatic sills: an experimental approach. *Tectonophysics* 489, 1–13. doi:10.1016/j.tecto.2010.03.004

Hagos, M., Konka, B., and Ahmed, J. (2016). A preliminary geological and generalized stratigraphy of western margin of northern Afar depression, Dallol Area, northern Ethiopia. *Momona Ethiop. J. Sci.* 8, 1–22. doi:10.4314/mejs.v8i1.1

Helenes, J., Carreño, A. L., and Marcos-Girón, R. Y. (2020). Miocene-Pliocene biochronology of the Obregón Basin and it's bearing on the evolution of the Proto-Gulf of California. *J. S. Am. Earth Sci.* 104, 102758. doi:10.1016/j.jsames.2020.102758

Holwerda, J. G., and Hutchinson, R. W. (1968). Potash-bearing evaporites in the Danakil area, Ethiopia. *Econ. Geol.* 63, 124–150. doi:10.2113/gsecongeo.63.2.124

Hurman, G. L., Keir, D., Bull, J. M., McNeill, L. C., Booth, A. D., and Bastow, I. D. (2023). Quantitative analysis of faulting in the Danakil Depression Rift of Afar: the importance of faulting in the final stages of magma-rich rifting. *Tectonics* 42, e2022TC007607. doi:10.1029/2022TC007607

Jackson, M. P. A., Cornelius, R. R., Craig, C. H., Gansser, A., Stöcklin, J., and Talbot, C. J. (1990). Salt diapirs of the Great Kavir, Central Iran. *Geol. Soc. Am. Mem.* 177, 1–150. doi:10.1029/2023GL10282610.1130/MEM177-p1

Keir, D., Pagli, C., Bastow, I. D., and Ayele, A. (2011). The magma-assisted removal of Arabia in Afar: evidence from dike injection in the Ethiopian rift captured using InSAR and seismicity. *Tectonics* 30, TC2008. doi:10.1029/2010TC002785

Kotopoulou, E., Delgado Huertas, A., Garcia-Ruiz, J. M., Dominguez-Vera, J. M., Lopez-Garcia, J. M., Guerra-Tschuschke, I., et al. (2019). A polyextreme hydrothermal system controlled by iron: the case of Dallol at the Afar Triangle. *ACS Earth Soace Chel* 3, 90–99. doi:10.1021/acsearthspacechem.8b00141

Laben, C. A., and Brower, B. V. (2000). *Process for enhancing the spatial resolution of multispectral imagery using pan-sharpening*. U. S. Patent 6,011,875.

Lalou, C., Nguyen, H. V., Faure, H., and Mareira, L. (1970). Datation par la méthode uranium-thorium des hauts niveaux de coraux de la dépression de l'Afar (Éthiopie). *Rev. Geogr. Phys. Geol. Dyn.* 12, 3–8.

La Rosa, A., Raggiunti, M., Pagli, C., Keir, D., Wang, H., and Ayele, A. (2023). Extensional earthquakes in the absence of magma in northern Afar: insights from InSAR. *Geophys. Res. Lett.* 50, e2023GL102826. doi:10.1029/2023GL102826

Leroy, S., Philippe, R., Julia, A., François, B., Elia d', A., Louise, W., et al. (2012). From rifting to oceanic spreading in the Gulf of Aden: a synthesis. *Arab. J. Geosci.* 5, 859–901. doi:10.1007/s12517-011-0475-4

López-García, J. M., Moreira, D., Benzerara, K., Grunewald, O., and López-García, P. (2020). Origin and evolution of the halo-volcanic complex of Dallol: proto-volcanism in northern Afar (Ethiopia). *Front. Earth Sci.* 17. doi:10.3389/feart.2019.00351

Master, S. (2016). Gaet'ale-a reactivated thermal spring and potential tourist hazard in the Asale salt flats, Danakil depression, Ethiopia. *J. Appl. Volcanol.* 5, 1. doi:10.1186/s13617-015-0042-x

Mastin, L. G., and Pollard, D. D. (1988). Surface deformation and shallow dike intrusion processes at inyo craters, long valley, California. *J. Geophys. Res.* 93, 13,221–13,235. doi:10.1029/JB093iB11p13221

Maurer, T. (2013). "How to pan-sharpen images using the Gram-Schmidt method – a recipe," in International Archives of the Photogrammetry, Remote Sensing and Spatial Information Sciences, Volume XL-1/W1, ISPRS Hannover Workshop 2013, Hannover, Germany, 21 – 24 May 2013.

McDermott, J. M., Parnell-Turner, R., Barreyre, T., Herrera, S., Downing, C. C., Pittoors, N. C., et al. (2022). Discovery of active off-axis hydrothermal vents at 9° 54'N East Pacific Rise. *Proc. Nat. Acad. Sci.* 119, e2205602119. doi:10.1073/pnas.2205602119

Mège, D., Purcell, P. G., Bézos, A., Jourdan, F., and La, C. (2015). "A major dyke swarm in the Ogaden region south of Afar and the early evolution of the Afar triple junction," in *Magmatic rifting and active volcanism 420*. Editors T. J. Wright, A. Ayele, D. J. Ferguson, T. Kidane, and C. Vye-Brown (London: Geol. Soc. London, Sp. Publ). doi:10.1144/SP420.7

Miller, N. C., and Lizzaralde, D. (2013). Thick evaporites and early rifting in the guaymas basin, Gulf of California. *Geology* 41, 283–286. doi:10.1130/G33747.1

Mitchell, N. C., Lii, M., Ferrante, V., Bonatti, E., and Rutter, E. (2010). Submarine salt flows in the central Red Sea. *Geol. Soc. Am. Bull.* 122, 701–713. doi:10.1130/B26518.1

Moore, C., Wright, T., Hooper, A., and Biggs, J. (2019). The 2017 eruption of Erta 'Ale volcano, Ethiopia: insights into the shallow axial plumbing system of an incipient mid-ocean ridge. *Geochem. Geophys. Geosystems* 20, 5727–5743. doi:10.1029/2019GC008692

Moors, H., De Craen, M., Smolders, C., Provoost, A., and Leys, N. (2023). The waterbodies of the halo-volcanic Dallol complex: earth analogs to guide us, where to look for life in the universe. *Front. Microbiol.* 14, 1134760. doi:10.3389/fmicb.2023.1134760

Mourgues, R., Gressier, J. B., Bodet, L., Bureau, D., and Gay, A. (2011). "Basin scale" versus "localized" pore pressure/stress coupling - implications for trap integrity evaluation. *Mar. Petroleum Geol.* 28, 1111–1121. doi:10.1016/j.marpetgeo.2010.08.007

Nobile, A., Pagli, C., Keir, D., Wright, T., Ayele, A., Ruch, J., et al. (2012). Dike-fault interaction during the 2004 Dallol intrusion at the northern edge of the Erta ale ridge (Afar, Ethiopia). *Geophys. Res. Lett.* 39, L19305. doi:10.1029/2012GL053152

Ogubazghi, G., Ghebreab, W., and Havskov, J. (2004). Some features of the 1993 Bada earthquake swarm of southeastern Eritrea. *J. Afr. Earth Sci.* 38, 135–143. doi:10.1016/j.jafrearsci.2003.12.002

Otálora, F., Palero, F., Papaslioti, E.-M., and García-Ruiz, J. M. (2022). Mineralochemical mechanism for the formation of salt volcanoes: the case of Mount Dallol (Afar Triangle, Ethiopia). *ACS Earth Space Chem.* 6, 2767–2778. doi:10.1021/acsearthspacechem.2c00075

Pelloux, A. (1927). The minerals of Vesuvius. *Am. Mineral.* 12, 14–21.

Pérez, E., and Chebude, Y. (2017). Chemical analysis of gaet'ale, a hypersaline pond in Danakil depression (Ethiopia): new record for the most saline water body on earth. *Aquat. Geochem.* 23, 109–117. doi:10.1007/s10498-017-9312-z

Ramírez-Zerba, N., Spelz, R. M., Yarbuh, I., Negrete-Aranda, R., Contreras, J., Clague, D. A., et al. (2022). Architecture and tectonostratigraphic evolution of the Pescadero Basin Complex, southern Gulf of California: analysis of high-resolution bathymetry data and seismic reflection profiles. *J. S. Am. Earth Sci.* 114, 103678. doi:10.1016/j.jsames.2021.103678

Rauche, H., and van der Klauw, S. (2015). *Technical report in support of disclosure of preliminary economic assessment for SOP production, Allana Potash Corp., Danakhil Project, Afar State, Ethiopia*. Erfurt, Germany: ERCOSPLAN, 268.

Rowan, M. G., Urai, J. L., Fiduk, J. C., and Kukla, P. A. (2019). Deformation of intrasalt competent layers in different modes of salt tectonics. *Solid earth.* 10, 987–1013. doi:10.5194/se-10-987-2019

Rubin, A. M., and Pollard, D. D. (1988). Dike induced faulting in rift zones of Iceland and Afar. *Geology* 16, 413–417. doi:10.1130/0091-7613(1988)016<0413:DIFIRZ>2.3.CO;2

Ruch, J., Keir, D., Passarelli, L., Di Giacommo, D., Ogubazghi, G., and Jónsson, S. (2021). Revealing 60 years of earthquake swarms in the southern Red Sea, Afar and the Gulf of aden. *Front. Earth Sci.* 9, 664673. doi:10.3389/feart.2021.664673

Rupnik, E., Daakir, M., and Pierrot Deseilligny, M. (2017). MicMac – a free, open-source solution for photogrammetry. *Softw. Stand.* 2, 14. doi:10.1186/s40965-017-0027-2

Sang, Y.-D., Adam, B. M. T., Li, C.-F., Huang, L., Wen, Y.-L., Zhang, J.-L., et al. (2023). Punctiform breakup and initial oceanization in the central Red Sea rift. *J. Mar. Sci. Eng.* 11, 808. doi:10.3390/jmse11040808

Sasvári, A., and Baharev, A. (2014). SG2PS (structural geology to postscript converter) - a graphical solution for brittle structural data evaluation and paleostress calculation. *Comput. Geosciences* 66, 81–93. doi:10.1016/j.cageo.2013.12.010

Schofield, N., Alsop, I., Warren, J., Underhill, J. R., Lehné, R., Beer, W., et al. (2014). Mobilizing salt: magma-salt interactions. *Geology* 42, 599–602. doi:10.1130/G35406.1

Szitkar, F., Dyment, J., Petersen, S., Bialas, J., Klischies, M., Graber, S., et al. (2019). Detachment tectonics at Mid-Atlantic Ridge 26°N. *Sci. Rep.* 9, 11830. doi:10.1038/s41598-019-47974-z

Talbot, C. J. (1978). Halokinesis and thermal convection. *Nature* 273, 739–741. doi:10.1038/273739a0

Talbot, C. J. (2008). Hydrothermal salt-but how much? *Mar. Petroleum Geol.* 25, 191–202. doi:10.1016/j.marpetgeo.2007.05.005

Tingay, M. R. P., Hillis, R. R., Morley, C. K., Swarbrick, R. E., and Okpere, E. C. (2003). "Pore pressure/stress coupling in Brunei Darussalam – implications for shale injection," in *Subsurface sediment mobilization 216*. Editors P. Van Rensbergen, Hillis, A. J. Maltman, and C. K. Morley (London: Geological Society, London, Special Publications), 369–379. doi:10.1144/GSL.SP.2003.216.01.24

Urai, J. L., Schléder, Z., Spiers, C. J., and Kukla, P. A. (2017). "Flow and transport properties of salt rocks," in *Dynamics of complex intracontinental basins: the Central European basin system*. Editors R. Littke, U. Bayer, D. Gajewski, and S. Nelskamp (Berlin: Springer), 277–290.

Urai, J. L., Spiers, C. J., Zwart, H. J., and Lister, G. S. (1986). Weakening of rock salt by water during long-term creep. *Nature* 324, 554–557. doi:10.1038/324554a0

Vereb, V., van Wyk de Vries, B., Hagos, M., and Karátson, D. (2020). Geoheritage and resilience of Dallol and the northern Danakil depression in Ethiopia. *Geoheritage* 12, 82. doi:10.1007/s12371-020-00499-8

Wan, Z., Hook, S., and Hulley, G. (2015). MOD11A1 MODIS/Terra Land surface temperature/emissivity daily L3 global 1km SIN grid V006. *Distrib. by NASA EOSDIS Land Process. DAAC*. Accessed 2020-06-23. doi:10.5067/MODIS/MOD11A1.006

Warren, J. K. (2015). *Danakhil potash; Ethiopia - modern hydrothermal and deep meteoric KCl, Part 3 of 4: salty matters*, 1–9. doi:10.13140/RG.2.1.4883.3443

Warren, J. K. (2016). *Evaporites. A geological compendium*. Cham: Springer, 1813. doi:10.1007/978-3-319-13512-0

Wolfenden, E., Ebinger, C., Yirgu, G., Deino, A., and Ayalew, D. (2004). Evolution of the northern Main Ethiopian rift: birth of a triple junction. *Earth Planet. Sci. Lett.* 224, 213–228. doi:10.1016/j.epsl.2004.04.022

Wright, T. J., Ebinger, C. E., Biggs, J., Ayele, A., Yirgu, G., Keir, D., et al. (2006). Magma-maintained rift segmentation at continental rupture in the 2005 Afar dyking episode. *Nature* 442, 291–294. doi:10.1038/nature04978

Xu, W., Xie, L., Aoki, Y., Rivalta, E., and Jónsson, S. (2020). Volcano-Wide deformation after the 2017 Erta ale dike intrusion, Ethiopia, observed with radar interferometry. *J. Geophys. Res.* 125, e2020JB019562. doi:10.1029/2020JB019562

Zhou, F., Dyment, J., Tao, J. H., and Wu, T. (2022). Magmatism at oceanic core complexes on the ultraslow Southwest Indian Ridge: insights from near-seafloor magnetics. *Geology* 50, 726–730. doi:10.1130/G49771.1

Supplementary Material

Tectonic and hydrothermal activity at the Yellow Lake fissure in response to the 2004 Dallol dyke intrusion event in Afar

Daniel Mège*, Ernst Hauber, Jérôme Dyment, Pascal Allemand, Hugo Moors, Mieke De Craen, Hanjin Choe

*** Correspondence:** Corresponding Author: dmege@cbk.waw.pl

Supplementary Figures

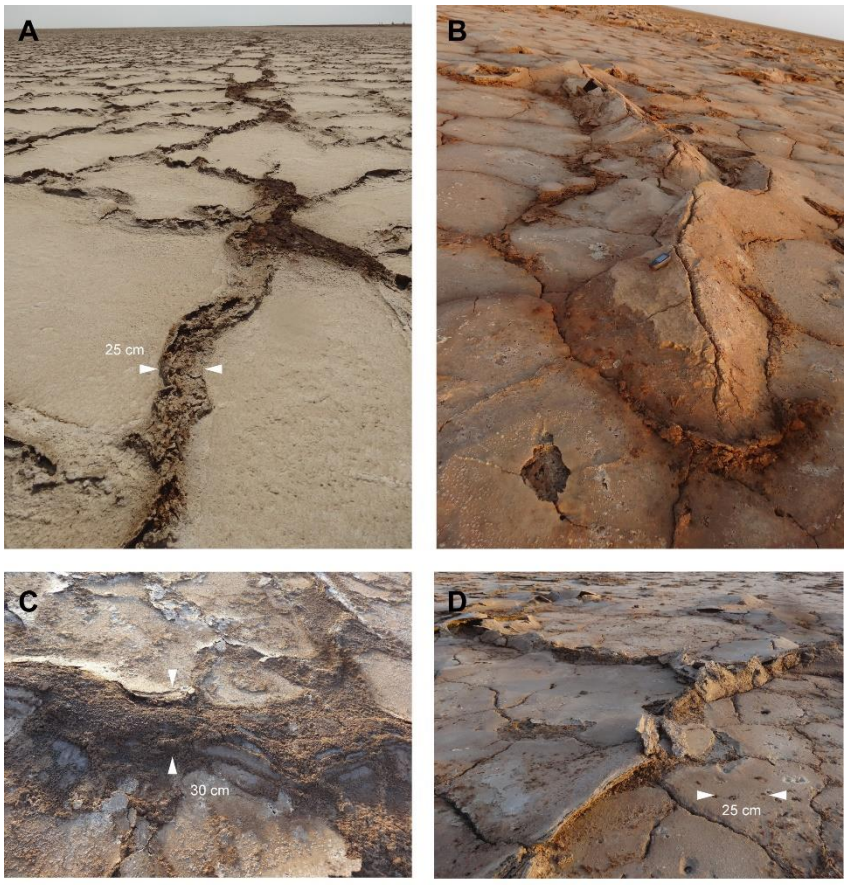

Supplementary Figure S1. Ridged landforms along the YLF. (**A**) Clay ridges in segment 2, which on satellite imagery can be mistaken for fresh open cracks; (**B**) Triangular-shaped, vertically inclined fractured salt polygons forming linear ridges in segment 3; (**C**) close view of a clay ridge in segment 3; (**D**) mixed clay and triangularly fractured plate morphology. (**A**) to (**C**) were photographed in January 2018. (**D**) was photographed in January 2019.

Supplementary Figure S2. Salt plate morphologies associated with subdued parts of YLF segments. (**A**) Expanded, diapiric clays at the junction between three plates; (**B**) circular holes with surrounding welded salt crystals; (**C**) circular holes with halo and contractional micro-ridges; (**D**) circular hole with associated fracture nucleation. Sites of type **C** and **D** are favourable to development of crystallised salt bubbles; (**E**) circular holes showing evidence of surges and halite recrystallization; a fragile white bubble with a thin salt crust is seen on the upper left; (**F**) cratered plate; (**G**) plate internal fracturing and fracture edge recrystallization of halite. On the left, plate edge geometry indicates probable formation by coalescence and enlargement of circular holes (dense circular hole alignments are indeed observed in some plates); (**H**) full dark clay platy resurfacing and spreading on salt plates. Salt plate morphologies associated with subdued parts of YLF segments, part 2. (**I**) Salt vent field along large YLF polygonal plates; (**J**) close view of a vent associated with platy dark mud resurfacing; (**K**) Large soft and sticky fractured polygonal plate along the YLF; (**L**) perhaps focusing on densely fractured zones along such plates, dark mud upflows emerge at surface. The radial patterns along the dark mud suggests forceful mud spreading at surface. Photographed in January 2018.

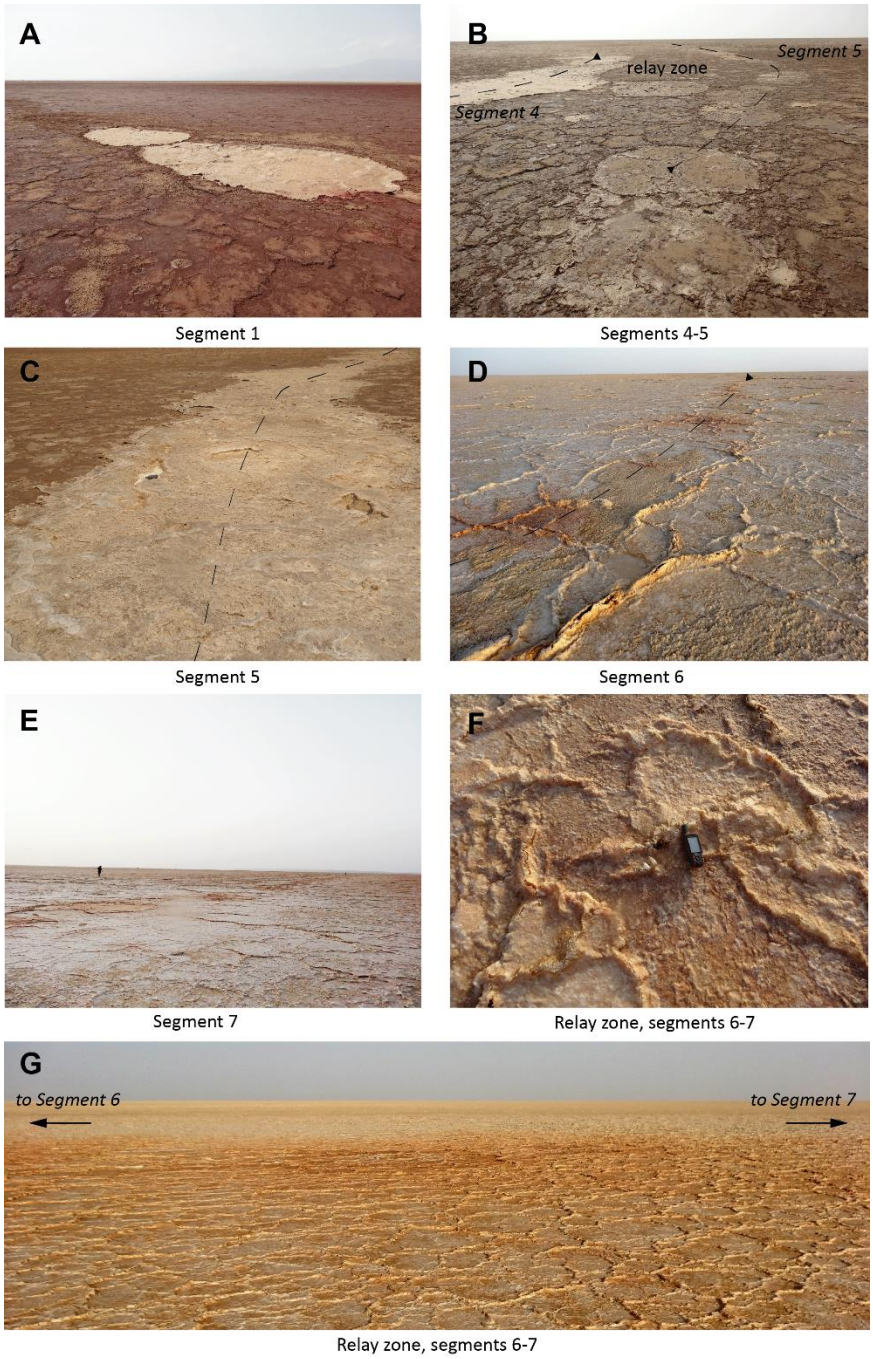

Supplementary Figure S3. Characteristic linear features of some segments. (**A**) View of the northernmost part of Segment 1, viewed to the South; (**B**) Relay zone between two *échelon* fissure segments in Segment 4, view toward South (14°12'47.73N, 40°19'24.9"E). Note the many small chimneys piercing the plates, as in Supplementary Figure S2A; (**C**) View to the South of Segment 5 next to the relay zone with Segment 4, showing small chimneys and salt brine pools (14°12'46.87"N, 40°19'25.36"E); (**D**) View of Segment 6 toward South (14°11'50"N, 40°19'.67"E); (**E**) View of segment 7 toward North (14°11'47.62"N, 40°19'48.22"E). Photographs taken in January 2019. The triangles indicate the end of segments. (**F**) View of the relay zone between segments – and 7 toward East. (**G**) Closer view on the relay zone area, containing native sulphur and salt bubbles. Photographs taken in January 2019.

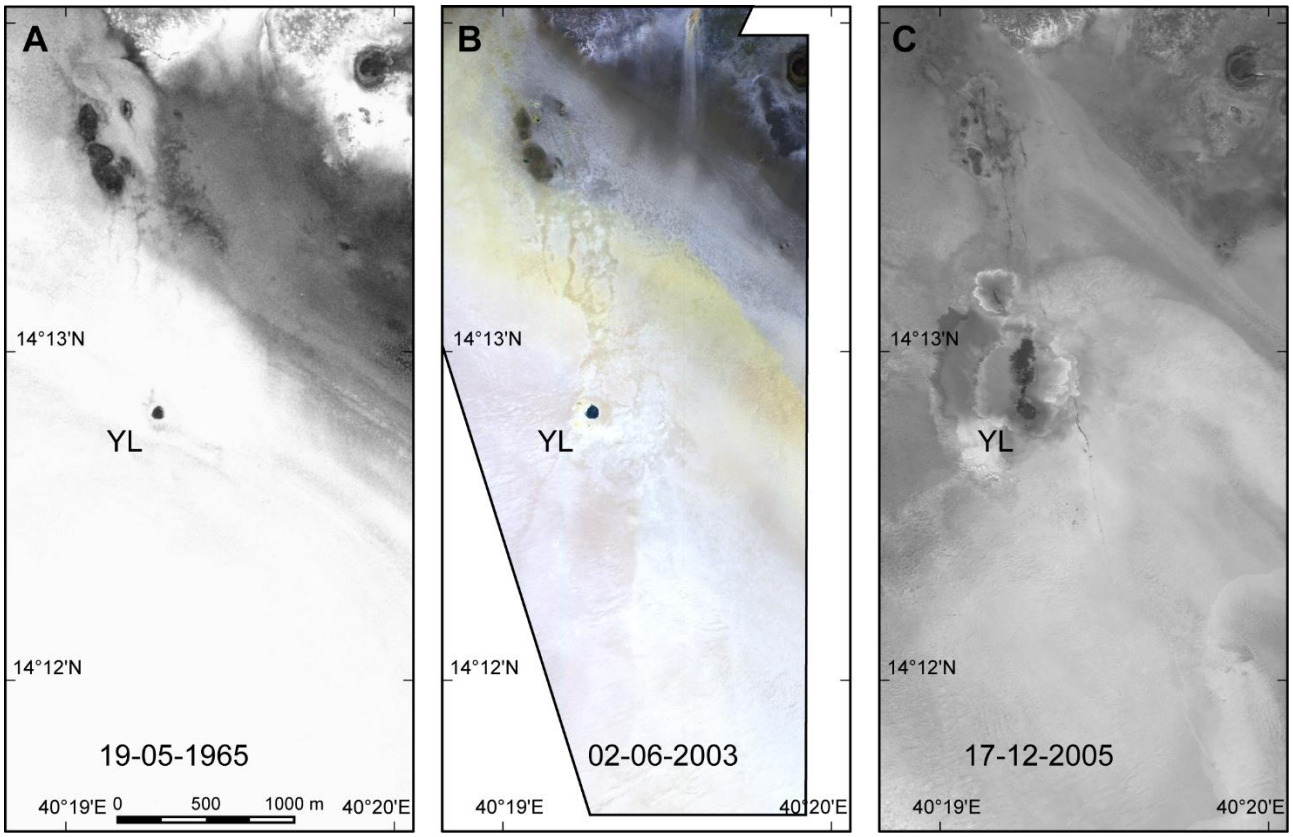

Supplementary Figure S4. Structural evolution of the Yellow Lake Fissure area since 1965. The black lines are fracture lines either exposed to the surface, along which pools are sometimes located, or linear salt plate edge alignments suggestive of deeper tension fracturing or fracturing at subcritical stress. YL stands for Yellow Lake. (**A**): fracturing already observed in 1965 by KeyHole 4-A (2.4m/pixel); (**B**): additional fracturing observed in 2003 by Quickbird-2 multispectral (2m/pixel; Gram-Schmidt pansharpened to 0.5 m/pixel). The red, green and blue channels correspond to the bands 4 (0.830 µm), 3 (0.560 µm) and 1 (0.485 µm), respectively; (**C**): fracturing observed since the first post-YLF high-resolution satellite image, by OrbView-3 (1m/pixel), in 2005.

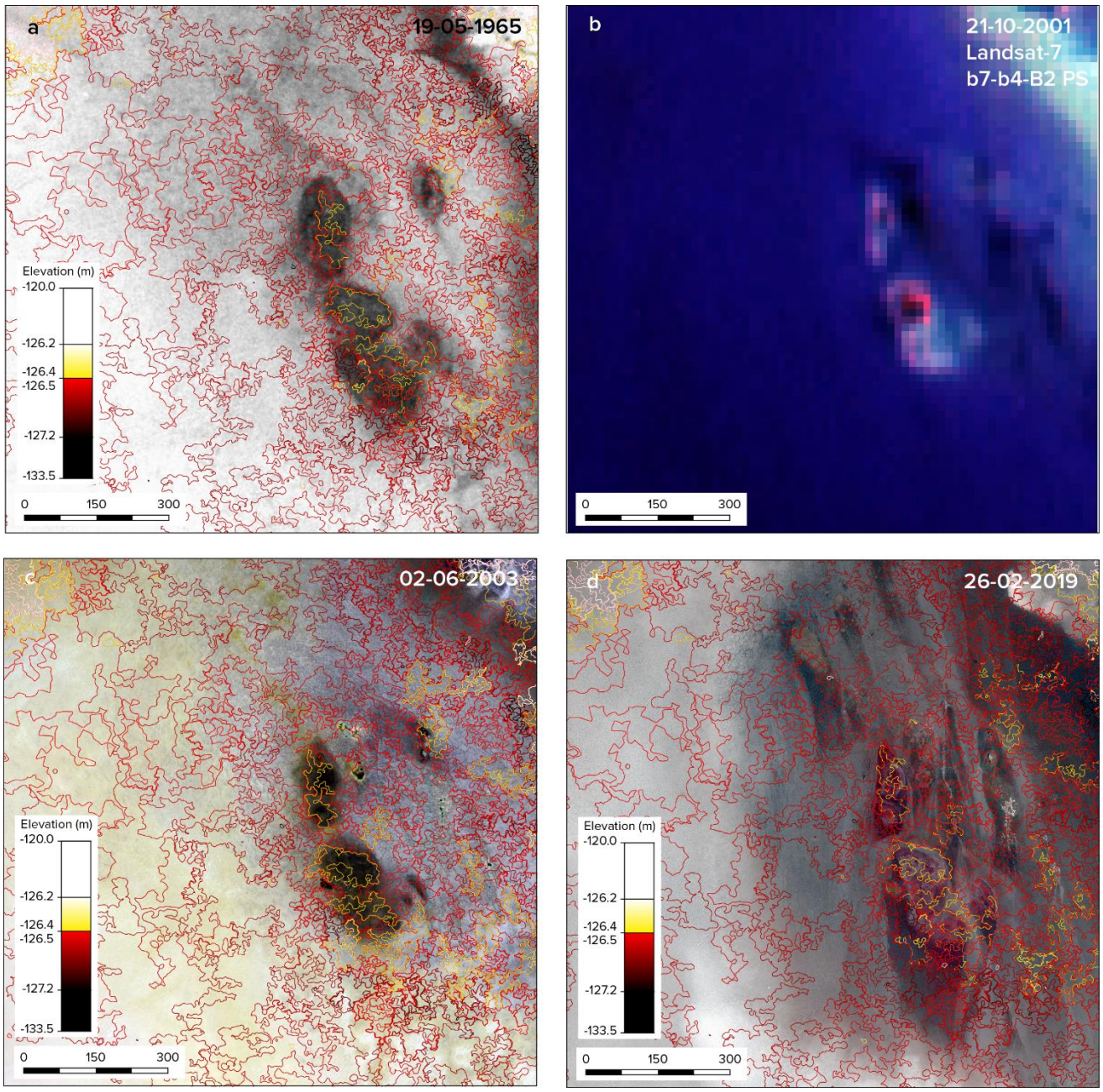

Supplementary Figure S5. Topographic evolution of the red salt patches through time. (**A**) The oldest image shows them already formed. Corona-4A image, 2.4m/pixel. (**B**) The red patches remain as islands during the October 2001 floods. Landsat-7 colour composite of bands 7 (red), 4 (green), and 2 (blue) of resolution 30m/pixel, with Gram-Schmidt pansharpening with Band 8 at 15m/pixel. (**C**) Red patch geometry remains unchanged in 2003 (Quickbird-2 image, 2.5m/pixel, with Gram-Schmidt sharpening with panchromatic band at 0.67m/pixel). (**C**) Similar observation is made in 2019 (Pleiades-1B, 2m/pixel with Gram-Schmidt sharpening using panchromatic band at 0.5m/pixel). In (**A**), (**C**), and (**D**), UAV-based topography is given with 0.1m-spaced contours. contours of length < 500 m were filtered.

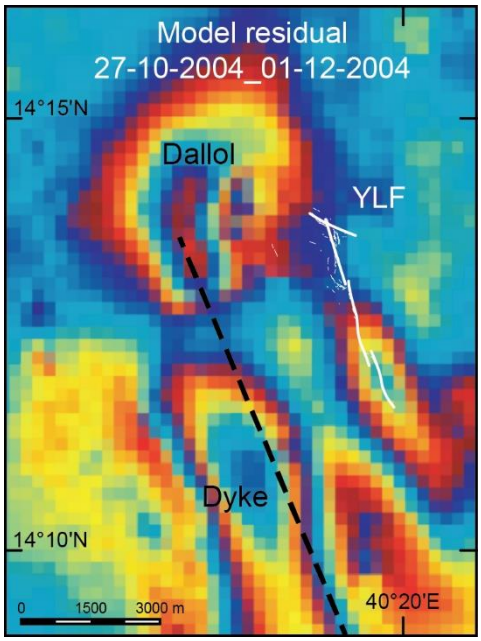

Supplementary Figure S6. Residual of InSAR-derived ground deformation field for the period 27-10-2004/01-12-2004, with the location of the YLF and the trace of the non-emergent Black Mountain dyke, modified after Nobile et al. (2012, extracted from Figure S5). The Black Mountain dyke is accounted for in the data, and is therefore not expected to be consistent with the deformation remaining in the residual. One fringe, from blue to red, is 2.81 cm vertically.

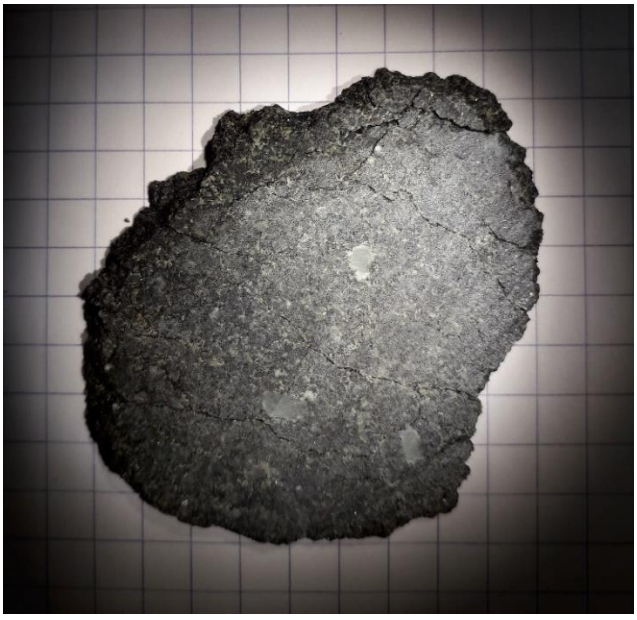

Supplementary Figure S7. Sawcut fragment of the dolerite sampled in a Mount Dallol salt dyke during the 2019 field campaign, exhibiting typical plagioclase phenocrysts. Location: 14°14'N, 40°17'E. By courtesy of Benjamin van Wyk de Vries. Chemical analyses are ongoing. Grid cells are 1 cm wide.

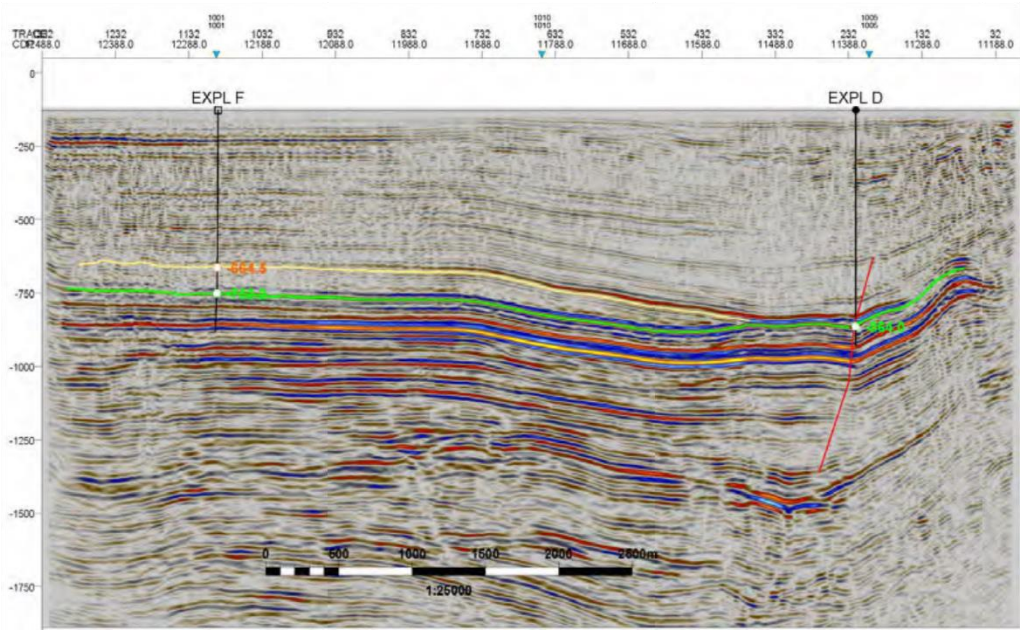

Supplementary Figure S8. Interpretation of a NNW-SSE trending migrated seismic cross-section in lake Asale north of Dallol (Environmental Resources Management Southern Africa (Pty) Ltd., 2014). The southern profile boundary (right) ends at the foot of Mont Dallol, toward which the sedimentary layers are increasingly upwarped. Exploratory boreholes EXPL D and EXPL F are located at 14.2624°N, 40.3018°E and 14.2982°N, 40.2859°E, respectively. EXPL D and the southern part of the profile are located in Figure 1. Vertical scale is in metres.

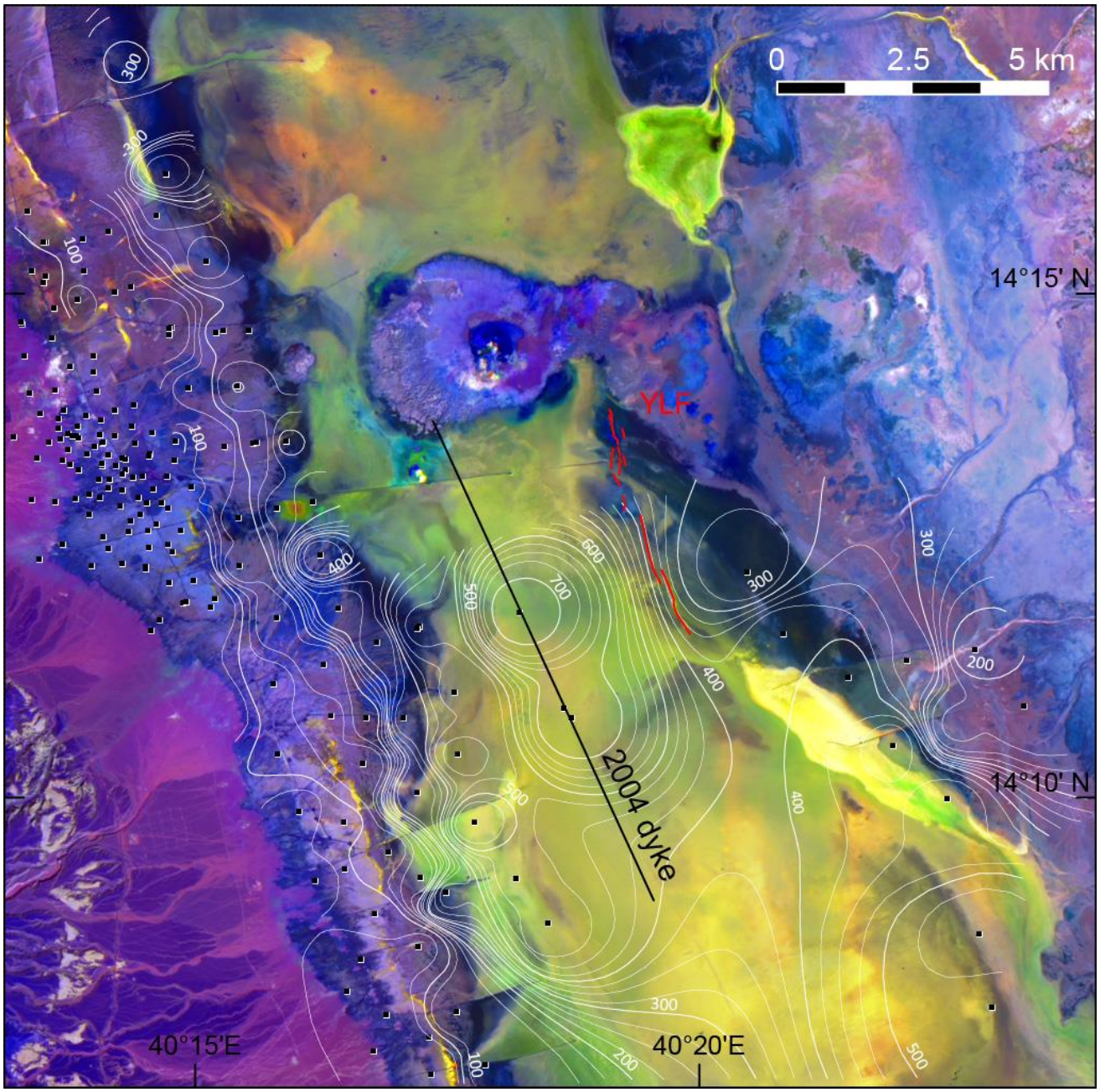

Supplementary Figure S9. Depth distribution of the Marker Beds, the uppermost part of the Houston Formation, in metres below the topographic surface. The depth is only constrained by drilling cores (black squares). The contours and drilling sites are from Rauche and van der Klauw (2015, Enclosure B). The location of the YLF and the coeval Black Mountain dyke is given. Note that the depth of the Marker Beds in the YLF area, although loosely constrained, is shallower than along the Black Mountain dyke and most of the drilled basin. The background image is a Gram-Schmidt pansharpened composite of bands 7 (2.220 μm), 4 (0.825 μm) and 2 (0.565 μm) of a Landsat-8 image acquired on 13-01-2018.

frontiers

Supplementary Material

Tectonic and hydrothermal activity at the Yellow Lake fissure in response to the 2004 Dallol dyke intrusion event in Afar

Daniel Mège*, Ernst Hauber, Jérôme Dyment, Pascal Allemand, Hugo Moors, Mieke De Craen, Hanjin Choe

*** Correspondence:** Corresponding Author: dmege@cbk.waw.pl

Supplementary tables

Date	Scene ID (Landsat-7)/Local granule ID (ASTER)
2004-08-26	LE71680502004239ASN01
2004-09-11	LE71680502004255ASN01
2004-09-27	LE71680502004271ASN01
2004-10-13	LE71680502004287ASN01
2004-11-14	LE71680502004319ASN00
2005-01-01	LE71680502005001PFS00
2005-01-17	LE71680502005017ASN00
2005-02-02	LE71680502005033ASN00
2005-02-18	LE71680502005049ASN00
2005-04-07	AST_L1T_00304072005075551_20150508235844_19664 and AST_L1T_00304072005075600_20150508235850_118442
2005-04-23	AST_L1T_00304232005075553_20150509044713_121936 and AST_L1T_00304232005075602_20150509044735_103448
2005-06-10	LE71680502005161ASN00
2005-07-28	LE71680502005209ASN00
2005-08-13	LE71680502005225ASN00
2005-08-29	LE71680502005241ASN00
2005-09-14	LE71680502005257ASN00
2005-09-30	LE71680502005273ASN00
2005-12-03	LE71680502005337SGS00

Supplementary Table S1. Description of the material used in Supplementary Video S1: Evolution of the YLF area between August 26th, 2004 and December 3rd 2005. The Landsat-7 image composites show bands 8 (red), 7 (green) and 5 (blue), and the ASTER image composites show band 1 (red), 6 (green) and 4 (blue).

Date	Satellite or mission	Product ID
1965-05-19	KeyHole-4A	DS1021-1009DA051
1972-05-08	KeyHole-4B	DS1117-2041DF151
2001-10-21	Landsat-7	LE71680502001294SGS00
2003-06-02	Quickbird-2	03JUN02074523-M2AS-012368508010_01_P002
2004-11-14	ASTER	AST_08_00311142004075459_20200406124521_16810
2005-01-19	ASTER	AST_08_00301092005193545_20200406124451_16620
2005-02-17	ASTER	AST_08_00302172005194137_20200406124451_16622
2005-12-17	OrbView-3	3v051217p0001021551a520005700852m_001625696_1GST
2012-11-15	Pleaides-1A	DS_PHR1A_201211150755134_SE1_PX_E040N14_0405_01880
2015-03-17	Spot-6	DS_SPOT6_201503170724335_FR1_FR1_FR1_FR1_E040N14_01709
2016-07-02	Pleiades-1B	DS_PHR1B_201607020802006_FR1_PX_E040N14_0306_04448
2016-11-20	WorldView-2	A010010600B3E700
2017-10-21	Pleaides-1A	DS_PHR1A_201710210751425_FR1_PX_E040N14_0403_04941
2018-01-13	Landsat-8	LC81680502018013LGN00
2019-01-24	Pleiades-1B	DS_PHR1B_201901240803060_FR1_PX_E040N14_0406_01048
2019-02-26	Pleiades-1B	DS_PHR1B_201902260758313_FR1_PX_E040N14_0406_01124

Supplementary Table S2. IDs of the other products used in this paper